

A Hybrid Update of the Fe-Si System by DSC, Thermodynamic Modeling and Statistical Learning from Ladle Refining Data of Electrical Steels



MICHAEL BERNHARD, DANIEL KAVIC, PETER PRESOLY, TAE-GYU WI, WON-BUM PARK, ROMAN RÖSSLER, ALFRED JUNGREITHMEIER, SERGIU ILIE, CHRISTIAN BERNHARD, and YOUN-BAE KANG

Electrical steels, also known as silicon steels, are essential materials in electrical applications due to their unique magnetic properties, which are enhanced by adding up to 3.5 wt pct Si. However, alloying with ferrosilicon FeSi75, a mixture of 25 wt pct Fe and 75 wt pct Si, during ladle refining faces steelmakers with metallurgical challenges, primarily due to the strong exothermic reaction during its dissolution in liquid steel. Here, solution thermodynamics of the Fe-Si system offer insights into the heat evolution and, therefore, superheating control for continuous casting. This study experimentally reassesses the binary Fe-Si system using Differential Scanning Calorimetry (DSC) and High-Temperature Laser Scanning Confocal Microscopy (HT-LSCM) to investigate phase equilibria between 0.50 and 12.50 wt pct Si and from 600 °C to 1550 °C. Thermodynamic modeling of the Fe-Si system was carried out in the CALPHAD framework, applying the Modified Quasichemical Model (MQM) for the liquid phase to consider the strong interactions between Fe and Si. In this way, the description of the liquid's mixing enthalpy and the activities of Fe and Si agree well with literature values. Deviations in liquidus and solidus temperatures, as measured by DSC, were reduced to within ± 5 °C. Additionally, the solubility limits of Fe and Si in intermediate silicides were refined based on the most recently published measurements. A comprehensive statistical analysis of industrial ladle refining processes involving 172 t ladles revealed a heat increase of 4.73 °C per t of FeSi75, consistent with adiabatic thermodynamic calculations (5 °C per t FeSi75). These findings improve the precision of thermodynamic databases and provide valuable insights for optimizing heat management and process control in producing silicon steels.

<https://doi.org/10.1007/s11663-024-03419-1>
© The Author(s) 2025

I. INTRODUCTION

ELECTRICAL or transformer steels are primarily made from silicon steels. They are essential for the global energy transition because of their unique magnetic properties, enhanced by the addition of up to 6.5 wt pct Si^[1] to the steel matrix. Increasing the Si content significantly improves the steel's magnetic properties, enabling rapid magnetization and demagnetization and reducing energy losses associated with hysteresis and eddy currents. Generally, Si steels can be divided into non-oriented (NGO) and grain-oriented (GO) grades. NGO silicon steels, with isotropic magnetic properties, are ideal for generator cores, electric motors, and electric meters applications.^[2] Conversely, GO Si steels, engineered for preferred magnetic orientation, excel in high-efficiency transformers and motors, important for minimizing energy losses.^[3]

MICHAEL BERNHARD is with the Chair of Ferrous Metallurgy, Montanuniversitaet Leoben, Franz-Josef-Strasse 18, 8700 Leoben, Austria and also with the Graduate Institute of Ferrous and Eco Materials Technology, Pohang University of Science and Technology, 77 Cheongamro, Pohang, Gyeongbuk 37673, Republic of Korea. Contact e-mail: michael.bernhard@unileoben.ac.at DANIEL KAVIC is with the K1-MET GmbH, Stahlstrasse 14, 4020 Linz, Austria and also with the Chair of Ferrous Metallurgy, Montanuniversitaet Leoben. PETER PRESOLY is with the Chair of Ferrous Metallurgy, Montanuniversitaet Leoben. TAE-GYU WI and WON-BUM PARK are with the Graduate Institute of Ferrous and Eco Materials Technology, Pohang University of Science and Technology. ROMAN RÖSSLER, ALFRED JUNGREITHMEIER, and SERGIU ILIE are with the voestalpine Stahl GmbH, voestalpine-Strasse 3, 4020 Linz, Austria. CHRISTIAN BERNHARD is with the Chair of Ferrous Metallurgy, Montanuniversitaet Leoben. YOUN-BAE KANG is with the Graduate Institute of Ferrous and Eco Materials Technology, Pohang University of Science and Technology and also with the Department of Materials Science and Engineering, Pohang University of Science and Technology, 77 Cheongamro, Pohang, Gyeongbuk 37673, Republic of Korea.

Manuscript submitted October 14, 2024; accepted December 16, 2024.

The production of Si steels presents steelmakers with challenging tasks. Si is usually added to the melt *via* ferroalloys during refining treatment. The alloy material contains around 75 pct Si by weight. Alloying leads to a considerable increase in the steel bath temperature inside the ladle due to the heat of the solution of the FeSi alloys. Typical literature values vary between 3×10^{-5} and $7.3 \times 10^{-5} \text{ }^\circ\text{C kg}^{-1}_{\text{FeSi}} \text{ t}^{-1}_{\text{steel}}$.^[4-6] Overheating can only be eliminated with increased effort until continuous casting. However, those data represent only empirical observations from steel plants, and no systematic analysis of the heating effect has been presented yet. In casting, the exact prediction of the liquidus temperature of high-alloyed Si steels is a key parameter for saving large amounts of energy by adjusting the superheat accurately. Further, the precise knowledge of the final solidification point plays a particularly important role in guaranteeing the quality of Si steels. For both the secondary metallurgy and casting process, the binary Fe-Si system represents the basis for thermodynamic data for process modeling, *e.g.*, enthalpy data for temperature modeling in secondary metallurgy^[7] and phase transformations temperatures required for solidification simulations.^[8,9]

The objective of the present study is to obtain new experimental data on melting equilibria and solid-state transformations at typical Si contents of electrical steel, and higher. Differential scanning calorimetry (DSC) and high-temperature laser scanning confocal microscopy (HT-LSCM) are employed to characterize the phase transformations in the temperature range of 600 to 1550 °C. In total, 9 alloys are prepared by high-frequency remelting (HFR) and spin casting technique carried out under Ar 5N (purity 99.999 pct) atmosphere. High-purity starting materials are used, and Si is alloyed in the composition range of 0.50 to 12.50 wt pct. Based on the new findings, the thermodynamic system is reassessed over the entire alloy range, whereby the modeling of the individual solution phases is partly adopted from the literature.^[10-12] The Gibbs energy of the liquid phase is formulated by the Modified Quasi-chemical Model (MQM)^[13,14] in the pair approximation, which leads to a better description of the thermodynamic properties, especially the enthalpy of mixing, of a melt with a tendency to short-range order (SRO).^[15,16] The Compound Energy Formalism (CEF)^[17,18] is used to describe the significant solubility of Si in bcc_A2 (ferrite, α - δ -Fe) and fcc_A1 (austenite, γ -Fe) as well as of Fe in diamond_A4 (solid Si). The ordering contribution of the bcc_B2 structure is adopted from the split-CEF description.^[10,11] The CEF is also applied to intermediate silicides (Fe₂Si, FeSi and β -FeSi₂).^[12] Other silicides with a defined chemical composition (Fe₅Si₃ and α -FeSi₂) are treated as stoichiometric compounds.

Finally, a hybrid approach^[19] is used to critically evaluate fundamental thermodynamic information with a comprehensive plant data analysis from voestalpine Stahl GmbH in Linz, to approximate the heat evolution during ladle refining of silicon steels due to the addition of ferroalloys. The actual phase stabilities in FeSi65 (Fe with 65 wt pct Si) and FeSi75 (Fe with 75 wt pct Si) are determined experimentally by X-ray diffraction (XRD)

method for the most practice-oriented calculation of ladle heating. Further, the chemical analysis of both ferroalloys (Fe and Si) is measured by inductively coupled optical emission spectroscopy (ICP-OES). The aim is to investigate a possible change of the Si content in ferrosilicon alloys to increase the process efficiency and to optimize the final temperature during ladle refining to improve the metallurgical conditions at the continuous caster.

II. LITERATURE REVIEW

An excellent literature review was given by Cui and Jung,^[11] so it is not the purpose of this section to repeat their work in detail. This section's objective is rather to work out possible improvements for a new thermodynamic description. However, for completeness, important thermodynamic data and phase diagram measurements available in the literature are briefly summarized in the first two sections. As the modeling of the bcc_D0₃ phase is not part of this study, experimental data relating to the bcc_D0₃ phase is not included in the literature section: here, we refer to.^[11] The crystallographic data of phases stable in the Fe-Si system are listed in Table I.

A. Thermodynamic Data

A large amount of data is available for the liquid's integral enthalpy of mixing (ΔH_{mix}) and/or partial enthalpies of mixing of Si and Fe (ΔH_{Si} , ΔH_{Fe}) in the liquid phase. Most of the measurements were carried out using calorimetry.^[20-30] Fruehan,^[31] Batalin and Sudavtsova^[32] and Sudavtsova *et al.*^[33] derived enthalpy data from their electromotive force measurements (EMF) between 1600 °C and 1650 °C using different cell designs. Zaitsev *et al.*^[34] determined ΔH_{Si} , ΔH_{Fe} and ΔH_{mix} at 1427 °C by Knudsen effusion mass spectrometry (KEMS).

The activities of Si and Fe (a_{Si} , a_{Fe}) in the melt were determined *via* EMF technique by various authors.^[31-33,35-37] Kubo and Sakao^[38] reduced SiO₂ by H₂ at 1560 °C to conclude on a_{Si} , whereas Zaitsev *et al.*^[34] and Miki *et al.*^[39] used KEMS in the temperature range of 1427 °C and 1420 °C to 1550 °C. Other methods were used by Chipman *et al.*^[40] (equilibrium distribution between liquid Fe and Ag, 1420 °C) and Hsu *et al.*^[41] (vapor pressure measurements, 1500 to 1600 °C). a_{Si} and a_{Fe} in the bcc_A2 phase were determined by Vecher *et al.*^[42] at 727 °C and by Sakao and Elliott^[43] between 1100 °C and 1350 °C using the EMF method.

The enthalpy of formation (ΔH_f^0) of Fe-Si solid alloys was measured calorimetrically in references.^[20,44-48] Bosholm *et al.*^[49] determined ΔH_f^0 for Fe₅Si₃, FeSi, α -FeSi₂, and β -FeSi₂ using a chemical transportation method. Vecher *et al.*^[42] derived ΔH_f^0 of Fe₃Si, FeSi, α -FeSi₂, and β -FeSi₂ from their EMF data. Numerous studies were performed to obtain the heat capacity

Table I. Summary of Stable Phases in the Binary Fe-Si System

Phase	Pearson Symbol	Space Group	Strukturbericht	Prototype	Model	Denoted in text
Liquid	—	—	—	—	MQM ^a	Liquid
γ -Fe	<i>cF4</i>	Fm $\bar{3}$ m	A1	Cu	CEF ^b	fcc_A1
(α, δ)-Fe	<i>cI2</i>	Im $\bar{3}$ m	A2	W	CEF	bcc_A2
α' -FeSi	<i>cP2</i>	Pm $\bar{3}$ m	B2	CsCl	CEF	bcc_B2
α'' -Fe ₃ Si	<i>cF16</i>	Fm $\bar{3}$ m	D0 ₃	BiF ₃	— ^c	bcc_D0 ₃
Fe ₂ Si	<i>hP6</i>	P63/mmc	—	Co _{1.75} Le	CEF	Fe ₂ Si
Fe ₅ Si ₃	<i>hP16</i>	P63/mcm	D88	Mn ₅ Si ₃	STCO ^d	Fe ₅ Si ₃
FeSi	<i>cP8</i>	P213	B20	FeSi	CEF	FeSi
α -FeSi ₂	<i>tP3</i>	P4/mmm	—	FeSi _{2_1}	STCO	α -FeSi ₂
β -FeSi ₂	<i>oC48</i>	Cmca	—	FeSi _{2_h}	CEF	β -FeSi ₂
Si(dia.)	<i>cF8</i>	Fd $\bar{3}$ m	A4	C(diam.)	CEF	Si (diamond_A4)

^aModified Quasichemical Model, ^bCompound Energy Formalism, ^cnot considered in the present work, ^dstoichiometric compound.

Table II. Thermodynamic Data in the Liquid Phase and bcc_A2 Solid Solutions Relevant for the Present Study

Quantity (Phase)	Method	X_{Si} (—)	T (°C)	Ref.
$\Delta H_{\text{mix}}, \Delta H_{\text{Si}}, \Delta H_{\text{Fe}}$ (Liquid)	calorimetry	0.10 to 0.90	1600	20
		0 (inf. dilution)	1600	21
		0 to 1	1525	22
		0 to 0.60	1600	23
		0 to 0.0742	1600	24
		0.006 to 0.0392	1700	25
		0 to 1	1427	26
		0.017 to 0.96	1650	27
		0 to 0.30	1600	28
		0.013 to 0.93	1600	29
		0 to 0.60	1492	30
		0 to 1	1600	31
		0.10 to 0.90	1600	32
		0.094 to 0.86	1600	33
		0.178 to 0.908	1427	34
$a_{\text{Si}}, a_{\text{Fe}}$ (Liquid)	EMF	0 to 1	1600	31
		0.10 to 0.90	1600	32
	KEMS	0.094 to 0.86	1600	33
		0.178 to 0.908	1427	34
		0 to 1	1600	31
		0.10 to 0.90	1600	32
		0.094 to 0.86	1600	33
		8×10^{-4} to 0.785	1530 \pm 15	35, 58
		0.10 to 0.90	1470 to 1510	36
		0.017 to 0.881	1470 to 1610	37
a_{Si} (bcc_A2)	KEMS	0.178 to 0.908	1427	34
		0.978 to 0.977	1420 to 1550	39
	Fe/Ag equilibration	0.144 to 0.558	1420	40
	Vapor pressure	0.01 to 0.988	1500 to 1600	41
	EMF	0.028 to 0.084	1100 to 1350	43

(C_{P})^[50–56] and to conclude on the standard Entropy at 25 °C (S_{298}°) by integration^[52–56] as well as on the heat content ($H_{\text{T}} - H_{298}$)^[51,53–57] of silicides.

The thermodynamic properties of the liquid phase, the bcc_A2 solid solution, and the stable silicides, which are relevant for the optimization procedure in this study, are listed in Tables II and III. A comprehensive summary is available in the work of Cui and Jung.^[11]

B. Phase Diagram Data

A large variety of experimental investigations on the overall Fe-Si system exists, including techniques of classic thermal analysis (TA), dilatometry, optical analysis (OA), magnetic analysis (MA), XRD,

metallography, equilibration and quenching (E&Q), differential thermal analysis (DTA) and DSC studies. Early studies were carried out already in the years 1905 to 1945,^[59–68] with ongoing research until 1974.^[69–76]

A comprehensive and widely accepted phase diagram of the Fe-side ($X_{\text{Si}} \leq 0.50$) was experimentally established by Schürmann and Hensgen^[77] using TA and equilibration technique. The bcc_A2/fcc_A1 solutions form a closed single-fcc_A1 region, generally known as “ γ -loop”.^[78] Phase equilibria in this region were investigated by TA,^[60,79] XRD^[80] and characterization techniques based on magnetic properties of bcc_A2/fcc_A1.^[81–83] The temperatures of bcc_A2/

bcc_B2 ordering were measured in references^[10,84–92] and their critical temperatures (T_C , Curie) were reported in references.^[61,65,67,76,79,84,85,87,93,94]

Tang and Tangstad^[95] studied melting equilibria on 200 the Si-rich side at $X_{Si} = 0.72$ –1 by TA. The solubility of Fe in solid Si (diamond_A4) was determined using radioisotopes,^[96] electron paramagnetic resonance (EPR)^[97–102] or deep level transition spectroscopy (DTLS).^[103] The homogeneity range of silicides was specifically studied by Abrikosov,^[104] Sidorenko *et al.*^[105,106] and Vainshtein *et al.*^[107]

The studies carried out most recently by Mecco and Napolitano^[108] and Han *et al.*^[109] are of special interest for the present assessment. Mecco and Napolitano^[108] carefully measured solid/liquid phase equilibria by DTA in the composition range of $X_{Si} = 0.05$ –0.30 by applying a heating rate (HR) variation to exclude the setup influence and to accurately extrapolate the phase transformation temperature to the equilibrium value. The concentration range investigated partly overlaps with the alloys studied by DSC in the present work (Sect. “III”). Hence, their data can be used to critically evaluate the results of the experimental section but, also, represent valuable data points in the thermodynamic optimization procedure. Han *et al.*^[109] provided new, comprehensive experimental information on the temperatures of liquidus, solidus, ordering in bcc, homogeneity range of silicides as well as on invariant reactions from $X_{Si} = 0.18$ –0.915. The concentration ranges of various silicides were determined by field-emission electron probe microanalysis with wavelength-dispersive X-ray spectrometers (FE-EPMA/WDS), while phase transformation temperatures at given composition were measured by DSC. These recently published high-quality data have not yet been included in any published modeling of the Fe-Si system.

The portion of experimental phase diagram data from the sources mentioned above, used in the present thermodynamic optimization, is listed in Table IV. For a detailed compilation of the methods, temperature ranges, and compositions from all the referenced literature, the authors refer to the compilation in the work of Cui and Jung.^[11]

C. Thermodynamic Assessments

An initial, comprehensive evaluation of the Fe-Si system was carried out by Chart.^[110,111] Then, the most widely known version of the phase diagram was published by Kubaschewski,^[112] which was based on the work of Chart^[111] and the investigations of Schürmann and Hensgen.^[77] Similar to the iron-rich region of the Fe-Al system,^[112–114] ferro-paramagnetic transitions and the ordering transformations A2/B2 and B2/D0₃ occur in the bcc solid solutions. The atomic order energy from disordered bcc (A2) to the CsCl-type (B2) and from B2 to the BiF₃-type (D0₃) was formulated by Lee *et al.*^[115] by integrating empirical specific heat capacity formulas.

At the beginning of the 1990s, Lacaze and Sundman^[116] optimized the Fe-Si system as part of the description of the ternary Fe-C-Si system. The transition from A2 to B2 was considered, but a description of the B2/D0₃ transformation was omitted for practical reasons. This version was subsequently used in most commercial thermodynamic databases. Miettinen^[117] slightly adjusted their proposed parameters for bcc_A2, fcc_A1 to avoid the formation of an inverse miscibility gap in the liquid and to improve the calculations of the ternary Fe-C-Si system.

In 2012, Ohnuma *et al.*^[10] experimentally and thermodynamically investigated all magnetic transitions and ordering phenomena in the bcc phase. A model for the ordered contribution of the D0₃ phase was proposed based on a four-sublattice model in the CEF framework. By that, the experimental data and literature sources of high-temperature phase equilibria could be successfully reproduced by providing a thermodynamic model over the whole composition range.

The most comprehensive assessment of the binary Fe-Si system, including an excellent literature review, was published by Cui and Jung^[11] in 2017. Two different sets of parameters were applied for the liquid phase: the Bragg-Williams model (BW) and the Modified Quasi-chemical model (MQM). In the first set, all order transformations were considered, whereby the optimization was carried out in Thermo-Calc.^[118] In the second set, the liquid was modeled using the MQM, but the bcc_B2/bcc_D0₃ transition could not be properly handled with Factsage.^[11] In all cases, the silicides were assumed to be stoichiometric. Other modifications were done by Yuan *et al.*^[119] by modeling the Fe-Si-Zn system and by Tang and Tangstad^[95] by studying the Si-rich part of the phase diagram.

In the framework of developing a steel database for Interdendritic Solidification (IDS) software,^[120,121] Miettinen *et al.*^[122] reassessed the description given in.^[117] They neglected the implementation of the B2 and D0₃ phases to speed up the calculations for solidification simulations of steel. However, the Gibbs energy contribution by A2/B2 ordering was added to the bcc_A2 model, which is evident from Figure 1(a). Most recently, Witusiewicz *et al.*^[12] published a thermodynamic description in the framework of modeling the Fe-Ni-Si system. The liquid phase was remodeled with a larger quantity of model parameters in the BW approach. A substantial improvement in the assessment was achieved by describing intermediate silicides (Fe₂Si, FeSi, β -FeSi₂) with the CEF to calculate their solubility range for Fe and Si accurately, see Figure 1(b). In Figures 1(a) and (b) the descriptions of Miettinen *et al.*^[122] and Witusiewicz *et al.*^[12] result in an inverted liquid miscibility gap at elevated temperatures. This is partially due to neglect of the Short-Range-Ordering (SRO) in the liquid phase. An example was shown by Shubhank and Kang^[123] for Fe-C binary liquid alloy, where an inverted liquid miscibility gap was reported in the previous modeling using the BW random mixing model for the liquid phase.^[124] The authors resolved this issue by using MQM which considers the SRO.

Table III. Thermodynamic Data of Fe-Si Solid Solutions and Silicides Relevant for the Present Study

Quantity	Method	$X_{\text{Si}} (-)$	T ($^{\circ}\text{C}$)	Ref.
$\Delta H_{\text{f}}^{\circ}$	calorimetry	0.33 to 0.70	25	20, 44
		0.33 to 0.70	25	45
		0.50	25	46
		0.50, 0.70	25	47
		0.50	25	48
	transportation method	0.375, 0.50, 0.667, 0.70	25	49
	EMF	0.25, 0.50, 0.667, 0.70	25, 727	42
S_{298}°	transportation method	0.375, 0.50, 0.667, 0.70	25	49
	calorimetry (C_{P} integration)	0.50, 0.667	25	52
		0.375, 0.50, 0.667, 0.70	25	53–56
$H_{\text{T}}-H_{298}$	calorimetry	0.50, 0.667	- 262 to 127	52
		0.375, 0.50, 0.667, 0.70	25	53–56
		0.50	850 to 1580	57

Table IV. Phase Diagram Information Relevant for the Present Study, Partly Taken from the Compilation of Cui and Jung^[11]

Type of Data	Method	$X_{\text{Si}} (-)$	Ref.
General Phase Diagram	FE-EPMA	< 0.20	10
	DTA, SEM, XRD, MA	0.10 to 0.40	76
	TA, DTA, Q&E	0 to 0.50	77
	TEM	0.096 to 0.156	89–91
	DTA	0.70 to 1	95
	DTA	0.05 to 0.30	108
	Fe-EPMA, DSC	0.18 to 0.915	109
bcc_A1/fcc_A1	XRD	0.018 to 0.036	80
	MA	0.014 to 0.042	81
T_{C} (bcc_A2, bcc_B2)	MA	0.012 to 0.037	82
	DTA, SEM, XRD, MA	0.10 to 0.40	76
Homogeneity of Silicides	DTA	0.05 to 0.30	108
	Fe-EPMA, DSC	0.18 to 0.915	109
Solubility of Fe in Diamond_A4*	DTA, SEM, XRD, MA	0.10 to 0.40	76
	radioisotopes	~ 1	96
	EPR	~ 1	97
		~ 1	98
		~ 1	99
		~ 1	100
		~ 1	101
	INAA	~ 1	102
	DTLS	~ 1	103

bcc_D0₃ ordering is excluded.

*Low solubility of Fe in diamond_A4 ($X_{\text{Fe}} \sim 10^{-7}$ – 10^{-10}).

A summary of CALPHAD-type assessments, their publication year, and thermodynamic models used to describe the individual phases stable in the Fe-Si system are summarized in Table V. Conclusions on the present modeling and possible improvements can be made as follows:

- The description of bcc_A2 is kept unchanged from Cui and Jung^[11] as experimental activity data of Si from Sakao and Elliott^[43] could be reproduced highly accurately. The bcc_B2 description is taken from Cui and Jung^[11] based on the model of Ohnuma *et al.*^[10] The fcc_A1 model parameters are adjusted to fit the new experimental data of the bcc_A2/fcc_A1 solid-state equilibria gained in the present work.
- The description of the silicides is adopted from the work of Witusiewicz *et al.*^[12] to describe the solubility range of Fe and Si in intermediate silicides. In this context, the most recent solubility data of Han *et al.*^[109] are considered for the first time, and the Gibbs energy of endmembers and excess parameters are changed to fit this data more precisely, if required.
- The MQM is used for the liquid phase to model the strong interaction between Fe and Si. The MQM parameters are optimized to fit the present DSC measurements of the bcc_A2/liquid phase boundaries with the highest agreement. Special focus is also placed on reproducing thermodynamic properties of the liquid phase, such as partial mixing enthalpies and partial excess Gibbs energies, which is discussed in detail in Sect. “V-B”. This step marks the most fun-

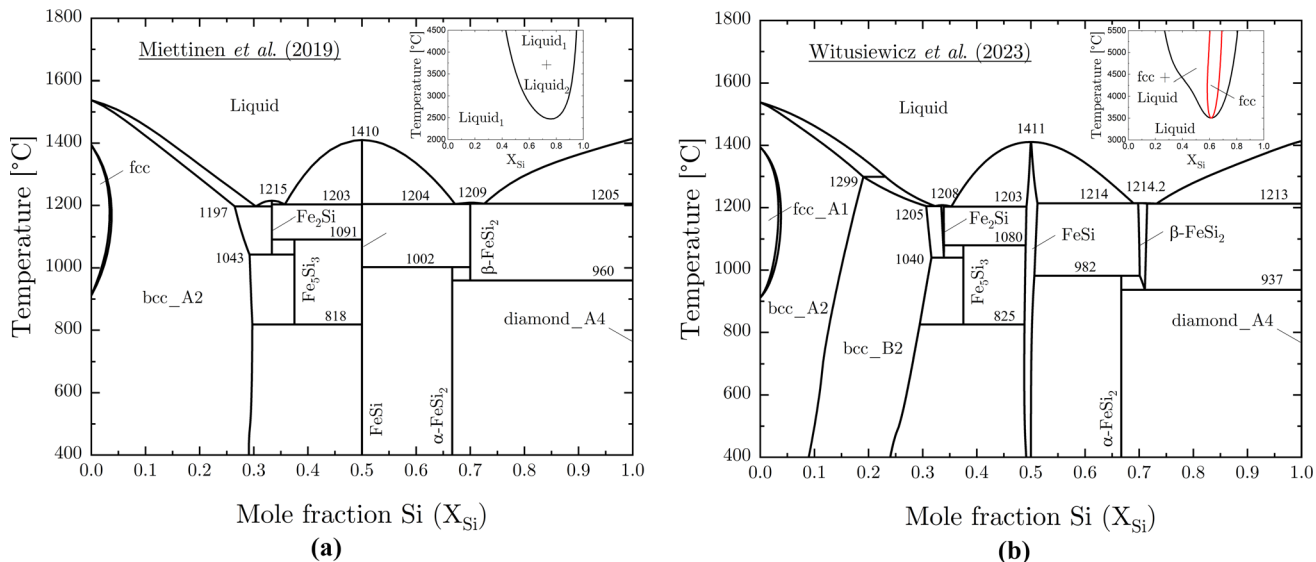


Fig. 1—Calculated phase diagrams according (a) Miettinen *et al.*^[122] and (b) Witusiewicz *et al.*^[12] Latter one was calculated with the provided thermodynamic database (tdb) file in Thermo-Calc software.^[118]

damental improvement of the present assessment for practical applications in refining and casting Si steels.

III. MATERIALS AND METHODS

A. Sample Preparation and Chemical Analysis

The samples for DSC analysis were produced in a high-frequency remelting (HFR) furnace “Lifumat-Met-3.3-Vac” from Linn High Therm GmbH (Eschenfelden, Germany). Technically pure iron cylinders (99.9 pct Fe) and silicon lumps (99.9999 pct Si, Alfa Aesar, LOT# 61000304) were used as starting materials. To guarantee controlled melting in the HFR process, a hole was drilled in the 50 g iron cylinders and filled with the amount of Si lumps according to the defined chemical composition. The melting process was carried out in Al_2O_3 crucibles under Ar 5N (purity 99.999 pct) over-pressure atmosphere. After two minutes of chemical and thermal homogenization by inductive bath movement, the melt was cast into a copper mold by centrifugation.^[78,125,126] The final chemical analysis of each sample was determined by an optical emission spectrometer (OES) of type QSG 750 from OBLF (Witten, Germany). The Si content and relevant trace element levels of all samples produced are summarized in Table VI.

B. Differential Scanning Calorimetry (DSC)

Differential scanning calorimetry (DSC) represents a widely used technique to record phase transformations associated with an exothermic or endothermic enthalpy change. Relevant information on the proper use of this method and the correct evaluation of DSC signals can be found in the NIST recommended practice guide.^[127] In previous studies of the authors, the application to

characterize the kinetics and equilibrium of solid-state phase transformations,^[78,126] and melting equilibria^[125,128–130] of Fe-based alloys was demonstrated.

In the present study, all measurements were carried out in a DSC of type 404F1 Pegasus (NETZSCH-Gerätebau GmbH, Selb, Germany) with an Rh furnace ($T_{\text{max}} = 1650$ °C). A Pt sensor and type S thermocouples were used. The DSC analysis was performed in Al_2O_3 crucibles (85 μL) with a lid; in each trial an empty crucible was the reference. The protective tube of the Rh furnace was continuously purged with Ar 5N (purity 99.999 pct), and a Zr getter was placed below the DSC sensor to minimize oxygen levels at elevated temperatures ($T > 350$ °C). Small samples of 50 mg mass were used for the experiments. The setup was calibrated by measuring the melting points of NETZSCH’s standards of pure metals In, Bi, Al, Ag, Au, Ni, and Co.

The DSC signal is significantly influenced by heating rate (HR) applied, the sample mass, and the enthalpy change occurring during the phase transformation. In particular, the end of a phase transformation, usually indicated by a “peak” in the signal, is shifted to higher values by high HRs, large sample masses, and significant heat changes, *e.g.* 13.81 kJ mol^{-1} ^[131] when melting Fe. Therefore, an accurate determination of the liquidus temperature is usually achieved by varying the HRs, and extrapolation to 0 °C s^{-1} yields the equilibrium temperature. When determining the onset of melting or for transformations with small enthalpy changes, *e.g.*, γ -Fe to δ -Fe with 0.826 kJ mol^{-1} ,^[131] the variation of the HR is usually omitted, and the average of several independent measurements is used as the result.

The procedure for varying HRs is time-consuming and costly, as numerous samples must be measured to create the section of a phase diagram. NETZSCH’s Tau-R software^[132] provides an efficient method to calculate equilibrium temperatures from a single

Table V. Summary of Popular CALPHAD Optimizations of the Fe-Si System and Thermodynamic Models Used

Authors	Year	Ref.	Liquid	A2/B2	B2/D0 ₃	Silicides
Lacaze and Sundman	1991	116	BW	yes	no	STCO
Ohnuma <i>et al.</i>	2012	10	BW	yes	yes	STCO
Cui and Jung	2017	11	BW	yes	yes	STCO
Cui and Jung	2017	11	MQM	yes	no	STCO
Miettinen <i>et al.</i>	2019	122	BW	no	no	STCO
Witusiewicz <i>et al.</i>	2023	12	BW	yes	no	CEF, STCO

Table VI. Chemical Composition of Samples Alloy Investigated

Alloy	X_{Si} (-)	Si (Wt Pct)	C (Wt Pct)	Mn (Wt Pct)	P (Wt Pct)	S (Wt Pct)
S-I	0.0099	0.50	0.005	0.026	0.0020	0.0014
S-II	0.0201	1.02	0.002	0.026	0.0021	0.0014
S-III	0.0395	2.02	0.006	0.062	0.0030	0.0052
S-IV	0.0562	2.90	0.007	0.033	0.0030	0.0037
S-V	0.0784	4.09	0.004	0.019	0.0037	0.0043
S-VI	0.0948	4.99	0.011	0.025	0.0021	0.0010
S-VII	0.1135	6.03	0.008	0.030	0.0030	0.0035
S-VIII	0.1629	9.49	0.012	0.027	0.0020	0.0033
S-IX	0.2202	12.40	0.010	0.024	0.0020	0.0029

Si contents are given in mole fraction (X_{Si}) for consistency with the modeling section and in weight percent (wt pct).

measurement. Within the present study, the Tau-R calibration is performed for the $10\text{ }^\circ\text{C min}^{-1}$ signal. Detailed arguments for selecting $10\text{ }^\circ\text{C min}^{-1}$ as a standard value in the scanning mode can be found in recent studies by the authors.^[125,130] For demonstration purposes, the Tau-R method is explained in Figure 2 based on the DSC analyses of alloy S-VI ($X_{Si} = 0.095$), which does not undergo a solid-state transformation from ferrite to austenite. Melting of ferrite (bcc_A2) proceeds in the temperature range of 1400 to 1500 °C. The DSC signals obtained during melting are plotted in Figure 2(a) depending on the applied HRs (5, 10 and $15\text{ }^\circ\text{C min}^{-1}$). As reported in literature,^[125,130] the onset remains approximately constant and T_S can be given as the average temperature of the three independent trials with 1438.3 °C. The peak shifts to higher temperatures at higher HR^[125,128,130] and the value of $T_L = 1469.3\text{ }^\circ\text{C}$ determined by the Tau-R method is in excellent agreement with the extrapolated equilibrium value of $T_L = 1468.4\text{ }^\circ\text{C}$ in Figure 2(b). The deviation is below the typical measurement error of the system applied ($\Delta T = \pm 2\text{ }^\circ\text{C}$); this similarly applies to T_S .

The full T-t cycle applied in the DSC is plotted in Figure 2(c), including the first (“slow”) and second (“fast”) measurement procedure for an alloy. In general, phase transformations are already determined in the first run. In contrast, selected sections with higher HR are scanned in the second cycle to shorten the test time and protect the equipment from possible failures. Furthermore, the second scan is used to reproduce the measurement results: at least two measurements are performed for each alloy.

C. High-Temperature Laser Scanning Confocal Microscopy (HT-LSCM)

In recent decades, high-temperature laser scanning confocal microscopy (HT-LSCM) has become an important technique in steel research for studying metallurgical processes *in situ* on a sample surface by combining laser scanning confocal optics and an infrared heating furnace. Examples include the investigation of the movement, aggregation and clustering of non-metallic particles in liquid steel,^[133–135] their dissolution in slags^[136] and at steel/slag interfaces,^[137,138] the observation of austenite decomposition during continuous cooling,^[126,139,140] the characterization of solidification of steel^[141,142] and crystallization of slags,^[143–145] the quantitative evaluation of grain growth processes^[146–149] and the coupling with DSC to establish phase diagrams for Fe-based alloys.^[78,125,128,150] Kern *et al.*^[151] showed that the observations on the sample surface also represent the bulk conditions.

As shown in Sect. “V-A”, the start of the ferrite/austenite transformation (bcc_A2 \rightarrow bcc_A2 + fcc_A1) is often barely visible in the DSC chart. In this case, HT-LSCM is a promising tool to gain further information on solid-state phase equilibria in the binary γ -loop. The specific use of HT-LSCM in this work follows the procedure applied to the Fe-P system in a recent work by M. Bernhard *et al.*^[78]

The experiments were carried out using an HT-LSCM type VL2000DX-SVF17SP from Lasertec (Yokohama, Japan) with a high-temperature furnace SVF17-SP from Yonekura (Yokohama, Japan). Small $5 \times 5 \times 1.5\text{ mm}$ samples were cut from alloys S-I and S-II listed in Table VI. The samples were ground and polished

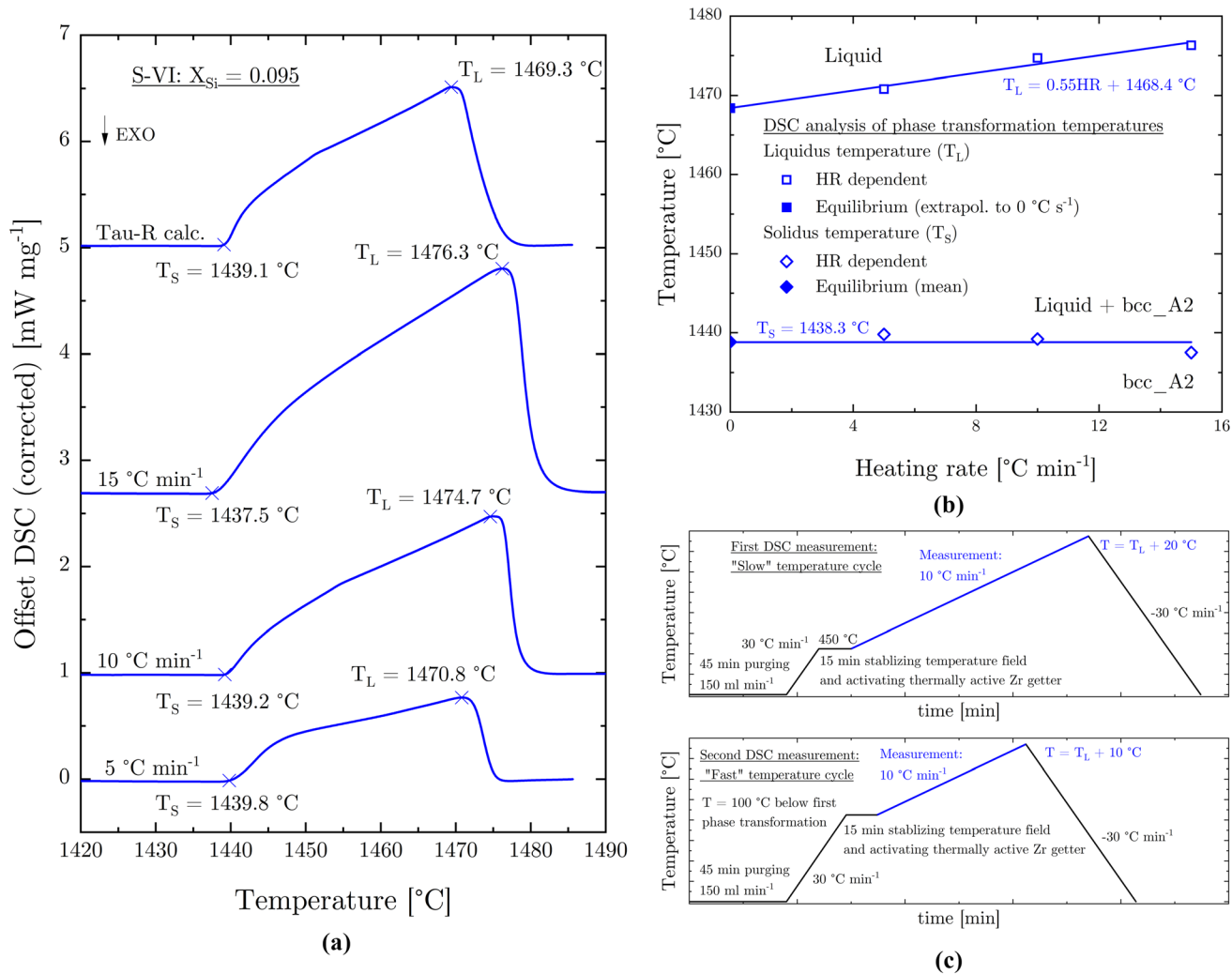


Fig. 2—DSC analysis of alloy S-VI ($X_{Si} = 0.095$). (a) DSC signals of melting for several HRs and the corresponding Tau-R calculation, (b) linear regression in a common HR variation to obtain the equilibrium value of T_L at $0^{\circ}\text{C min}^{-1}$ and (c) detailed t-T program applied in the DSC analysis.

according to the standard procedure. Afterward, they were placed on the sample holder; the furnace chamber was evacuated and purged with Ar 5N (99.999 pct purity). Both samples were heated to 850°C at $600^{\circ}\text{C min}^{-1}$ followed by 15 minutes of isothermal holding, after which the nucleation of austenite in the ferrite matrix was observed in situ at a heating rate of $10^{\circ}\text{C min}^{-1}$. The HR corresponded to the DSC measurements described in Sect. “III-B”. The final temperature was set at 1050°C . After reaching the maximum temperature, controlled cooling to room temperature was carried out at a defined cooling rate of $-400^{\circ}\text{C min}^{-1}$ under Ar atmosphere.

The temperature in the furnace chamber was monitored with a type S thermocouple at the bottom of the sample holder. To obtain accurate temperatures on the sample surface, temperature referencing had to be performed before each experimental campaign using an external thermocouple welded to the sample’s surface.^[146] During the experiment, a video was recorded with a maximum frame rate of 60 s^{-1} so that the phase

transformation starting and finishing temperatures could be determined post-experimentally as all microstructural changes had become clearly visible due to the thermal etching effect.^[78]

Figures 3(a) and (b) show selected images of the HT-LSCM video of sample S-I. In the micrograph, the areas where fcc_A1 is stable are already marked in color for better optical visibility. The fraction of fcc_A1 on the sample’s surface ($f_{\text{fcc_A1}}$) can be easily determined from the marked region, considering the entire image section. M. Bernhard *et al.*^[78] showed that $f_{\text{fcc_A1}} \sim 3$ pct is representative of the overall phase transformation temperature. For S-I, the determined phase equilibrium temperature bcc_A2/bcc_A2 + fcc_A1 is 920°C . As expected, austenite forms at the ferrite grain boundaries, and growth into the ferrite grain proceeds by a diffusional mechanism. The proportion of fcc_A1 already increases significantly at a slightly higher temperature of 932°C (11 pct) in the two-phase region bcc_A2 + fcc_A1. Similar observations can be obtained in Figures 3(c) and (d) for the case of sample S-II.

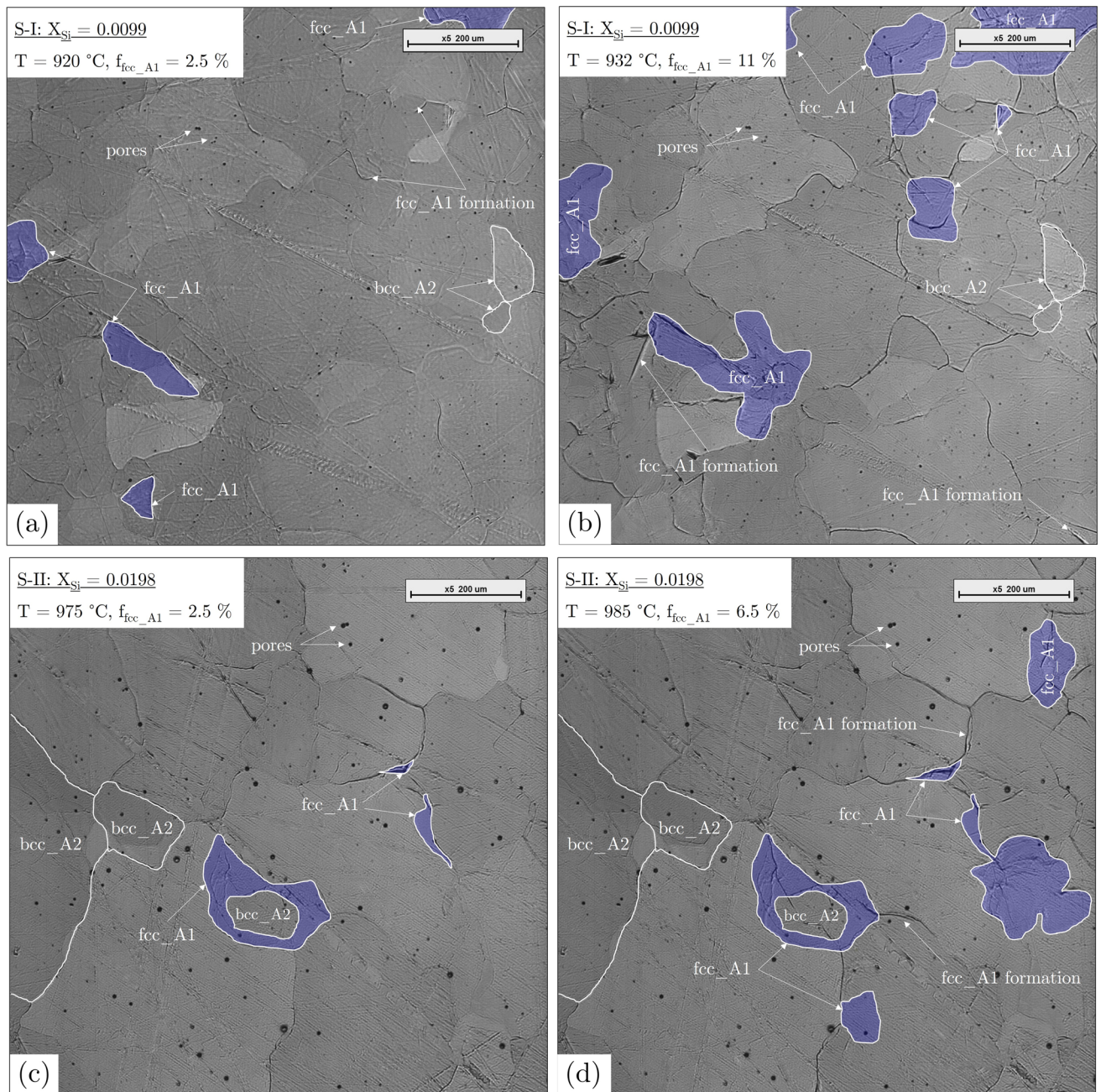


Fig. 3—HT-LSCM observations of bcc_A2/fcc_A1 transformation. (a), (b) sample S-I ($X_{Si} = 0.0099$) at 920 °C and 932 °C and (c), (d) sample S-II ($X_{Si} = 0.0198$) at 975 °C and 985 °C. For a better overview, the images were partly edited with Gimp GNU Image Manipulation Software.^[152]

Corresponding to the calculated phase diagrams in Figure 2, the nucleation temperature of fcc_A1 (975 °C) increases with higher Si content. Due to the wider temperature range of this alloy's bcc_A2 + fcc_A1 region, the fraction of fcc_A1 increases more slowly during scanning. Note that pores may result from the sample production by HFR.

IV. THERMODYNAMIC MODELS

All calculations in the assessment procedure were performed with FactSage 8.3 thermochemical software.^[131] The Gibbs energies of pure Fe and Si were adopted from the SGTE data of Dinsdale.^[153] The model parameters used or optimized in the present assessment are listed in Table VII.

Table VII. Thermodynamic Model Parameters Used or Optimized

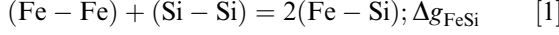
Phase	Model Parameters	Ref.
Liquid (Fe,Si)	$Z_{FeFe}^{Fe} = Z_{SiSi}^{Si} = Z_{FeSi}^{FeSi} = Z_{FeFe}^{Fe} = 6$	PW
bcc_A2 (Fe,Si) ₁ (Va) ₃	$\Delta G_{FeSi} = -35564 + 5.975T + (-16736 - 1.255T)X_{FeFe} + (4476.9 + 4.393T)X_{FeFe}^2 + (836.8 + 1.506T)X_{SiSi}$ $G_{Fe:Va} = GHSERFE$	[11]
bcc_B2 (Fe,Si) _{0.5} (Fe,Si) _{0.5} (Va) ₃	$G_{Si:Va} = GBCCSI$ $L_{Fe:Si:Va} = -154013.56 + 32.29T$ $L_{Fe:Si:Va} = -63511.47 + 13.25T$ $L_{Fe:Si:Va} = 35727.58$ $T_{C(Fe:Si:Va)} = Y_{Fe}^{Fe}1043 + Y_{Fe}^{Si}504(Y_{Fe}^{Fe} - Y_{Si}^{Si})$ $\Delta G_m^{ord} = -10464.8$	[10, 11]
fcc_A1 (Fe,Si) ₁ (Va) ₁	$G_{Fe:Va} = GFCCFE$	[11], PW
Si (Fe ₃ Si)	$G_{Si:Va} = GFCCSI$ $L_{Fe:Si:Va} = -115337.7 - 2.148T$ $L_{Fe:Si:Va} = -84776.9 + 44.33$ $L_{Fe:Si:Va} = 20007$ $g_{Fe}^{\circ} = GFCCFE + 1000$	[11], PW
Fe ₂ Si (Fe) ₁ (Fe,Va) ₁ (Va,Si) ₁	$g_{Si}^{\circ} = GHSERSI$ $L_{Fe:Si} = 117152 + 0.837T$ $g_{Fe:Fe:Si}^{Fe_2Si} = 2GHSERFE + GHSERSI - 72562.37 - 11.585T$ $g_{Fe:Si:Va}^{Fe_2Si} = 2GHSERFE + 15000$ $g_{Fe:Va:Va}^{Fe_2Si} = GHSERFE + 15000$ $g_{Fe:Si}^{Fe_2Si} = GHSERFE + GHSERSI + 35000$ $L_{Fe:Fe:Va:Si} = -94794.4 + 2.452T$	[12], PW
Fe ₅ Si ₃ (Fe) ₅ (Si) ₃	$S_{298}^{\circ} = 225.75$ $C_p(T > 273.15) = 180.30693 + 0.085911943T - 1060721.6T^{-2} + 2.6645942 \times 10^{-7}T^2$ $T_{Fe:Si} = 360$ $\beta_{Fe:Si}^{Fe_5Si_3} = 2.32$ $\Delta H_{f,298}^{\circ} = -211887.1$	[12], PW
FeSi (Fe,Si) _{0.5} (Fe,Si) _{0.5}	$g_{FeSi}^{FeSi} = GHSERFE + 7500$ $g_{FeSi}^{FeSi} = GHSERSI + 21000$ $g_{FeSi}^{FeSi} = -44218.53 + 142.92T - 24.285T \ln T + 107055T^{-1} - 0.003681T^2 + 1.4593 \times 10^{-7}T^3$ $L_{Fe:Fe:Si} = -2448 + 8.07T$ $\Delta H_{f,298}^{\circ} = -83779.33$	[12], PW
α -FeSi ₂ (Fe) ₁ (Si) ₂	$S_{298}^{\circ} = 61.354$ $C_p(T > 273.15) = 79.0299 - 0.0181458T - 999009.06T^{-2} + 1.782594 \times 10^{-5}T^2$	[12], PW
β -FeSi ₂ (Fe,Si) _{0.3} (Fe,Si) _{0.7}	$g_{\beta-FeSi_2}^{\beta-FeSi_2} = 0.7GHSERFE + 0.3GHSERSI + 5000$ $g_{\beta-FeSi_2}^{\beta-FeSi_2} = -30866.23 + 127.5829T - 21.4218T \ln T + 117285.345T^{-1} - 0.005496T^2 + 3.8389 \times 10^{-7}T^3$ $g_{\beta-FeSi_2}^{\beta-FeSi_2} = GHSERSI + 10000$ $L_{Fe:Fe:Si} = -44163.2$	[12], PW

Data for pure Fe and Si in respective reference states are taken from the work of Dinsdale.^[153] All quantities are given in J mol⁻¹ or J mol⁻¹ K⁻¹.
PW present work.

A. Liquid Phase

The MQM in the pair approximation was applied to describe the Gibbs energy of the liquid phase. This model has been successfully used to formulate the Gibbs energy of metal/metal, metal/semi-metal and metal/non-metal systems with relevance to steel.^[123,129,154–157] Kang^[158] recently discussed its working principle compared to the Bragg-Williams random mixing model. A detailed description of the MQM can be found in the work of Pelton *et al.*^[13,14] Here, only the essential background is summarized.

In the pair approximation for a binary solution consisting of Fe and Si atoms, the following pair exchange reaction on the sites of a quasi-lattice is considered:



where $(i-j)$ represent the first nearest neighbor pair and Δg_{AB} is the non-configurational Gibbs free energy change forming two moles of $(i-j)$ pairs. If n_{Fe} and n_{Si} are the numbers of moles Fe and Si, n_{ij} is the number of $(i-j)$ pairs and Z_{Fe} and Z_{Si} are the coordination numbers of Fe and Si, then the following mass balances are considered:

$$Z_{Fe}n_{Fe} = 2n_{FeFe} + n_{FeSi} \quad [2]$$

$$Z_{Si}n_{Si} = 2n_{SiSi} + n_{FeSi} \quad [3]$$

The pair fractions (X_{ij}), mole fractions (X_i) and coordination-equivalent (Y_i) fractions are defined as:

$$X_{ij} = n_{ij}/(n_{FeFe} + n_{SiSi} + n_{FeSi}) \quad [4]$$

$$X_{Fe} = n_{Fe}/(n_{Fe} + n_{Si}) = 1 - X_{Si} \quad [5]$$

$$\begin{aligned} Y_{Fe} &= Z_{Fe}n_{Fe}/(Z_{Fe}n_{Fe} + Z_{Si}n_{Si}) \\ &= Z_{Fe}X_{Fe}/(Z_{Fe}X_{Fe} + Z_{Si}X_{Si}) = 1 - Y_{Si} \end{aligned} \quad [6]$$

The Gibbs energy of the solution is given by:

$$G = (n_{Fe}g_{Fe}^{\circ} + n_{Si}g_{Si}^{\circ}) - T \Delta S^{\text{config}} + (n_{FeSi}/2)\Delta g_{FeSi} \quad [7]$$

where g_{Fe}° and g_{Si}° are the molar Gibbs energies of pure Fe and Si and ΔS^{config} is the configurational entropy of mixing given by randomly distributing the (Fe-Fe), (Si-Si) and (Fe-Si) pairs in the one-dimensional Ising approximation:^[159]

$$\begin{aligned} \Delta S^{\text{config}} &= -R(n_{Fe}\ln X_{Fe} + n_{Si}\ln X_{Si}) \\ &\quad - R[n_{FeFe}\ln(X_{FeFe}/Y_{Fe}^2) + n_{SiSi}\ln(X_{SiSi}/Y_{Si}^2) \\ &\quad + n_{FeSi}\ln(X_{FeSi}/2Y_{Fe}Y_{Si})] \end{aligned} \quad [8]$$

The Δg_{FeSi} may be expanded in terms of pair fractions:

$$\Delta g_{FeSi} = \Delta g_{FeSi}^0 + \sum_{i \geq 1} g_{FeSi}^{i0} X_{FeFe}^i + \sum_{j \geq 1} g_{FeSi}^{0j} X_{SiSi}^j \quad [9]$$

where Δg_{FeSi}^0 , g_{FeSi}^{i0} and g_{FeSi}^{0j} are the model parameters which can be functions of temperature.

The equilibrium pair distribution is determined by setting

$$(\partial G / \partial n_{FeSi})_{n_{Fe}, n_{Si}} = 0 \quad [10]$$

which leads to the equilibrium constant for the pair formation in Reaction (1) when the coordination number and the pair formation energy are constant, respectively, as it was used in the original model of Guggenheim:^[160]

$$X_{FeSi}^2 / (X_{FeFe}X_{SiSi}) = 4 \exp(-\Delta g_{FeSi} / RT) \quad [11]$$

When Δg_{FeSi} varies with pair fractions as given in Eq. [9], the form of Eq. [11] changes. Please refer to the recent article by Waldner.^[161]

The composition of maximum SRO is defined by the ratio of the coordination numbers Z_{Si}/Z_{Fe} , where each coordination number is given in the following equations:

$$\frac{1}{Z_{Fe}} = \frac{1}{Z_{FeFe}^{Fe}} \left(\frac{2n_{FeFe}}{2n_{FeFe} + n_{FeSi}} \right) + \frac{1}{Z_{FeSi}^{Fe}} \left(\frac{n_{FeSi}}{2n_{FeFe} + n_{FeSi}} \right) \quad [12]$$

$$\frac{1}{Z_{Si}} = \frac{1}{Z_{SiSi}^{Si}} \left(\frac{2n_{SiSi}}{2n_{SiSi} + n_{FeSi}} \right) + \frac{1}{Z_{SiFe}^{Si}} \left(\frac{n_{FeSi}}{2n_{SiSi} + n_{FeSi}} \right) \quad [13]$$

where Z_{FeFe}^{Fe} and Z_{FeSi}^{Fe} are the values of Z_{Fe} when all neighbors of Fe are Fe and when all nearest neighbors of Fe are Si, respectively, and where Z_{SiSi}^{Si} and Z_{SiFe}^{Si} are defined similarly. Z_{FeSi}^{Fe} and Z_{SiFe}^{Fe} represent the same quantity and are interchangeable.

B. bcc_A2, fcc_A1 and Si Disordered Solid Solutions

The bcc_A2 and fcc_A1 disordered solid solutions were modeled by the CEF^[17,18] with two sublattices. Fe and Si are located on the substitutional sites, while vacancies (Va) occupy the interstitial sites. The formulation by the CEF will allow the implementation of the current thermodynamic description into multicomponent steel databases, including interstitially dissolved C. However, if all the sites in all but one of the sublattices are vacant, the CEF reduces to the Bragg-Williams (BW) model of random mixing.^[17] The BW model was intentionally used to describe the Si solid solution in a single lattice. For all phases, the following formulation of the Gibbs energy equation is valid

$$G_m = (X_{Fe}g_{Fe}^{\circ} + X_{Si}g_{Si}^{\circ}) + RT(X_{Fe}\ln X_{Fe} + X_{Si}\ln X_{Si}) + X_{Fe}X_{Si}\sum_{v \geq 0} L_{Fe,Si}^v (X_{Fe} - X_{Si})^v \quad [14]$$

where X_i and g_i° are the molar fraction and the molar Gibbs energy of the pure component i in the corresponding reference state. $L_{Fe,Si}^i$ represent the adjustable model parameters, which can be a function of temperature. In case of bcc_A2 and fcc_A1, the contribution due to magnetic ordering (g_m^{mo}) based on the Hillert-Jarl approach was added.^[162]

C. bcc_B2 Ordering Contribution

The ordering contribution due to the bcc_B2 structure was adopted from the original split-CEF description of Ohnuma *et al.*^[10] with modification done by Cui and Jung.^[11] The total molar Gibbs energy of the bcc phase is given by^[10]

$$G_m^{bcc} = G_m^{bcc-A2}(X_i) + \Delta G_m^{ord} = G_m^{bcc-A2}(X_i) + G_m^{bcc-B2}(y'_i, y''_i) - G_m^{bcc-B2}(y'_i = X_i, y''_i = X_i) \quad [15]$$

where $G_m^{bcc-B2}(y'_i, y''_i)$ is the Gibbs energy of bcc phase formulated in the two-sublattice compound energy model and $G_m^{bcc-B2}(y'_i = X_i, y''_i = X_i)$ has the same mathematical form as $G_m^{bcc-B2}(y'_i, y''_i)$ in the special condition of $y'_i = X_i, y''_i = X_i$, representing the disordered state. y'_i and y''_i are the site fractions of Fe and Si on the first (') and second (") sublattice. Therefore, ΔG_m^{ord} becomes null when the bcc phase becomes disordered. Ohnuma *et al.*^[10] implemented the ordering contribution of bcc_B2 structure in such a way that the Gibbs energy of the disordered phase is not present in the ΔG_m^{ord} . Under the condition $G_m^{bcc-B2}(y'_i, y''_i) - G_m^{bcc-B2}(y'_i = X_i, y''_i = X_i) = 0$ it follows for the model parameters:

$$G_{Fe:Fe}^{bcc} = G_{Si:Si}^{bcc} = 0 \quad [16]$$

$$G_{Fe:Si}^{bcc} = G_{Si:Fe}^{bcc} = \Delta G_m^{ord} \quad [17]$$

$${}^0L_{Fe:Fe,Si}^{bcc} = {}^0L_{Fe,Si:Fe}^{bcc} = {}^0L_{Si:Fe,Si}^{bcc} = {}^0L_{Fe,Si:Si}^{bcc} = -\Delta G_m^{ord} \quad [18]$$

D. Intermediate Phases: Fe₂Si, FeSi and β -FeSi₂

Silicides showing a substantial mutual solubility of Fe and Si were modeled by the CEF^[17] according to the sublattice structure as proposed by Witusiewicz *et al.*^[12]

FeSi and β -FeSi₂ were considered as (Fe,Si)_a(Fe,Si)_b, respectively. The molar Gibbs energy is formulated by

$$G_m = y'_{Fe}y''_{Fe}g_{Fe:Fe}^{\theta} + y'_{Fe}y''_{Si}g_{Fe:Si}^{\theta} + y'_{Si}y''_{Si}g_{Si:Si}^{\theta} + y'_{Si}y''_{Fe}g_{Si:Fe}^{\theta} + aRT(y'_{Fe}\ln y'_{Fe} + y'_{Si}\ln y'_{Si}) + bRT(y''_{Fe}\ln y''_{Fe} + y''_{Si}\ln y''_{Si}) + ex G_m^{\theta} \quad [19]$$

where the excess Gibbs energy is given by

$$ex G_m^{\theta} = y'_{Fe}y'_{Si}y''_{Fe}L_{Fe,Si:Fe}^{\theta} + y'_{Fe}y'_{Si}y''_{Si}L_{Fe,Si:Si}^{\theta} + y'_{Fe}y''_{Fe}y''_{Si}L_{Fe:Fe,Si}^{\theta} + y'_{Si}y''_{Fe}y''_{Si}L_{Si:Fe,Si}^{\theta} + y'_{Fe}y'_{Si}y''_{Fe}y''_{Si}L_{Fe,Si:Fe,Si}^{\theta} \quad [20]$$

θ stands for the respective phase (FeSi, β -FeSi₂). $g_{i;j}^{\theta}$ and $g_{i;i}^{\theta}$ represent the endmembers. a and b are the stoichiometric coefficients, given for FeSi as $a = b = 0.5$ and for β -FeSi₂ as $a = 0.3$ and $b = 0.7$, respectively. The adjustable parameter L can be a function of temperature.

A 3-sublattice model was used for the more complex Fe₂Si solution with the sublattice formula^[12] (Fe)₁(Fe,-Va)₁(Va,Si)₁, yielding to the following expression of the molar Gibbs energy:

$$G_m = y''_{Fe}y''_{Si}y'''_{Fe:Fe,Si}g_{Fe:Fe,Si}^{Fe_2Si} + y''_{Fe}y''_{Va}y'''_{Fe:Fe,Va}g_{Fe:Fe,Va}^{Fe_2Si} + y''_{Va}y''_{Va}y'''_{Va:Va}g_{Va:Va}^{Fe_2Si} + y''_{Va}y''_{Si}y'''_{Si:Va,Si}g_{Si:Va,Si}^{Fe_2Si} + RT(y''_{Fe}\ln y''_{Fe} + y''_{Va}\ln y''_{Va} + y''_{Si}\ln y''_{Si}) + ex G_m^{Fe_2Si} \quad [21]$$

with

$$ex G_m^{Fe_2Si} = y''_{Fe}y''_{Va} \left(y'''_{Va}L_{Fe:Fe,Va:Va}^{Fe_2Si} + y'''_{Si}L_{Fe:Fe,Va:Si}^{Fe_2Si} \right) + y''_{Va}y''_{Si} \left(y'''_{Fe}L_{Fe:Fe:Va,Si}^{Fe_2Si} + y'''_{Va}L_{Fe:Va:Va,Si}^{Fe_2Si} \right) + y''_{Fe}y''_{Va}y''_{Si}y'''_{Si}L_{Fe:Fe,Va:Si}^{Fe_2Si} \quad [22]$$

Please note that the notation is identical to the given equations for the two-sublattice model of FeSi and for β -FeSi₂ but include a third sublattice (").

E. Stoichiometric Compounds: Fe₅Si₃ and α -FeSi₂

The silicides Fe₅Si₃ and α -FeSi₂ were treated as stoichiometric compounds. The molar Gibbs energy was modeled temperature-dependent and is given by

$$G_m = \Delta H_{298}^{\circ} + \int_{298}^T C_{Pd}dT - T \left[S_{298}^{\circ} + \int_{298}^T (C_P/T)dT \right] \quad [23]$$

where ΔH_{298}° is the standard enthalpy of formation relative to the standard states of pure Fe and Si at 25 °C and 1 bar. S_{298}° is the standard entropy at 298 K (25 °C) and C_P denotes the temperature-dependent heat capacity.

V. RESULTS AND DISCUSSIONS

The analysis in the following sections separates into the experimental analysis of phase equilibria by DSC/HT-LSCM performed in the present work and the improvement of the thermodynamic description using the MQM for the liquid phase in comparison to the most recent thermodynamic assessment from the literature.^[11,12,122] For the thermodynamic calculations, FactSage 8.3^[131] was used. However, in selected cases, Thermo-Calc 2024^[118] was utilized to perform the simulations using the thermodynamic database (tdb) file, provided by Witusiewicz *et al.*^[12]

A. Experimental Results of Phase Equilibrium Temperatures

The numerical values of phase transformation temperatures obtained with DSC and HT-LSCM are summarized in Table VIII. The graphical representation of the DSC measurement signals is shown in Figure 4(a). The critical temperature (T_C) of bcc_A2 decreases with rising Si content. For the bcc_A2/fcc_A1 equilibrium, plotted in Figure 4(c), only the end of the phase transformation ($T_{A2/A1,E}$) in the range of 900 to 1000 °C could be determined using the DSC method. The fcc_A1 nucleation ($T_{A2/A1,S}$) was optically observed with the HT-LSCM and corresponds to 920 °C at $X_{Si} = 0.0099$ and 975 °C at $X_{Si} = 0.0201$. In the high-temperature range, all relevant phase transformations could be analyzed using DSC, as the enthalpy change is more significant in these cases and the transformation kinetics are enhanced. The fcc_A1/bcc_A2 transformation ($T_{A1/A2,S}$) at $X_{Si} = 0.0099$ is 1368.7 °C, and at $X_{Si} = 0.0201$ it corresponds to 1333 °C. At $X_{Si} = 0.2202$, the alloy is already in the peritectic range, and the solidus temperature (T_S) and the peritectic phase transformation (T_P) are evident in the DSC graph. For samples with $X_{Si} = 0.0099$ – 0.1629 , the DSC charts show a sharp onset of the solidus temperature and a clearly pronounced peak in the liquidus temperature (T_L). At T_S and T_L , a continuous temperature drop can be recognized with increasing Si content, which generally agrees with the calculations in Figure 4(b). However, most thermodynamic calculations for the bcc_A2/liquid phase equilibrium temperature deviate significantly. This is particularly the case of Si contents up to $X_{Si} = 0.0395$, which declares the maximum Si content of electrical steels, in the modeling of Cui and Jung^[11] and Miettinen *et al.*^[122] Good agreement with the BW model can be observed using the parameters of Witusiewicz *et al.*^[12] However, the high number of excess parameters in the BW model leads to a polynomial course of the enthalpy of mixing in the infinitely dilute solution of Si, as will be discussed in the following sections, as well as to an inverse mixing gap in the liquid phase, see Figure 1(b). Therefore, revised modeling of the Gibbs energy of the liquid phase is necessary.

B. Thermodynamic Modeling of the Fe-Si System

Figure 5 shows the enthalpy properties of the Fe-Si liquid phase. In general, all previous assessments^[10–12,122] represent the integral enthalpy of mixing (ΔH) in Figure 5(c) with satisfying accuracy. A closer look at the partial enthalpy of Si (ΔH_{Si}) in Figure 5(a) leads to the conclusion that most previous assessments predict an unreliable course at $X_{Si} < 0.10$. The experimental data of^[23,27–29,34] show a consistent S-shaped trendline of ΔH_{Si} , whereas a straight decrease of ΔH_{Si} when $X_{Si} \rightarrow 0$ is predicted using the assessments given in references.^[11,122] The thermodynamic optimization of Witusiewicz *et al.*^[12] required many excess parameters to describe the liquid's Gibbs energy. The quantitative values at $X_{Si} \rightarrow 0$ correspond to his measurements reported in,^[29] but adding numerous parameters from ${}^0L_{FeSi}(X_{Fe} - X_{Si})^0$ up to ${}^5L_{FeSi}(X_{Fe} - X_{Si})^5$ to the excess Gibbs energy term in the BW formalism leads to a polynomial ΔH_{Si} curve at low amount of Si, see Figure 5(a).

In the present study, the MQM parameters proposed by Cui and Jung^[11] were chosen as initial values for the optimizations. It is evident from the integral enthalpy of mixing in Figure 5(c) that the composition of maximum SRO corresponds to $X_{Si} = 0.50$. Keeping, therefore, the coordination numbers $Z_{FeFe}^{Fe} = Z_{SiSi}^{Si} = 6$ and $Z_{FeSi}^{Si} = Z_{FeSi}^{Fe} = 6$ unchanged is reasonable. By comparing our proposed parameters for $\Delta g_{FeSi}^0 = -35564 + 5.975T$ J mol⁻¹ with the equation of Cui and Jung^[11] ($\Delta g_{FeSi}^0 = -33710.49 + 2.26T$ J mol⁻¹) the assessed Δg_{FeSi}^0 term is nearly identical. When $X_{Si} \rightarrow 0$ (or $X_{Fe} \rightarrow 0$), the experimental values of ΔH_{Si} and ΔH_{Fe} in infinite dilution ($\Delta H_{Si}^\infty, \Delta H_{Fe}^\infty$) significantly scatter. Therefore, it is an important step to select the reliable data of the partial enthalpy of mixing in the present modeling. This is also practically important as ΔH_{Si}^∞ is principally responsible for the exothermic reaction when ferrosilicon alloy is added to liquid steel. Enthalpy data ($\Delta H, \Delta H_{Si}, \Delta H_{Fe}$) provided by Gel'd *et al.*^[27] was considered the most reliable as their measurements were performed by direct calorimetry. In the composition range of $X_{Si} = 0.10$ – 0.90 , the reported results are consistent with the calorimetry performed by Woolley and Elliott^[23] and with data of Zaitsev *et al.*^[34] derived from the Knudsen-cell effusion method.

The inclusion of this data in the optimization procedure also provides the best alignment with practical observations obtained from extensive temperature measurements during the ladle refining of silicon steel (see Sect. “VI”). While the CALPHAD framework traditionally excludes process data from thermodynamic assessments, the present study takes a novel approach by combining experimental data from literature with insights derived from big data analytics. This hybrid methodology enables a more accurate prediction of thermodynamic properties, phase diagrams, and real-world plant behavior. This comprehensive approach ensures reliable modeling of ΔH_{Si}^∞ , which is critical for understanding the exothermic reactions that occur when ferrosilicon alloy is added to liquid steel.

Table VIII. Chemical Composition and Results of DSC Analysis and HT-LSCM Observations of Fe-Si Alloys

Sample	X_{Si} (-)	T_C (°C)	$T_{A2/A1,S}$ (°C)	$T_{A2/A1,E}$ (°C)	$T_{A1/A2,S}$ (°C)	$T_{A1/A2,E}$ (°C)	T_P (°C)	T_S (°C)	T_L (°C)
S-I	0.0099	767.4	920	950.2	1368.7	1379.1	—	1526.8	1535.4
S-II	0.0201	763.6	975	996.5	1333.0	1340.0	—	1519.7	1529.5
S-III	0.0395	754.1	—	—	—	—	—	1500.9	1514.3
S-IV	0.0562	744.8	—	—	—	—	—	1485.5	1501.7
S-V	0.0784	728.1	—	—	—	—	—	1460.6	1482.2
S-VI	0.0948	717.3	—	—	—	—	—	1438.8	1468.4
S-VII	0.1135	702.0	—	—	—	—	—	1415.2	1456.2
S-VIII	0.1629	647.2	—	—	—	—	—	1323.3	1392.6
S-IX	0.2202	—	—	—	—	—	1295.3	1263.1	1308.1

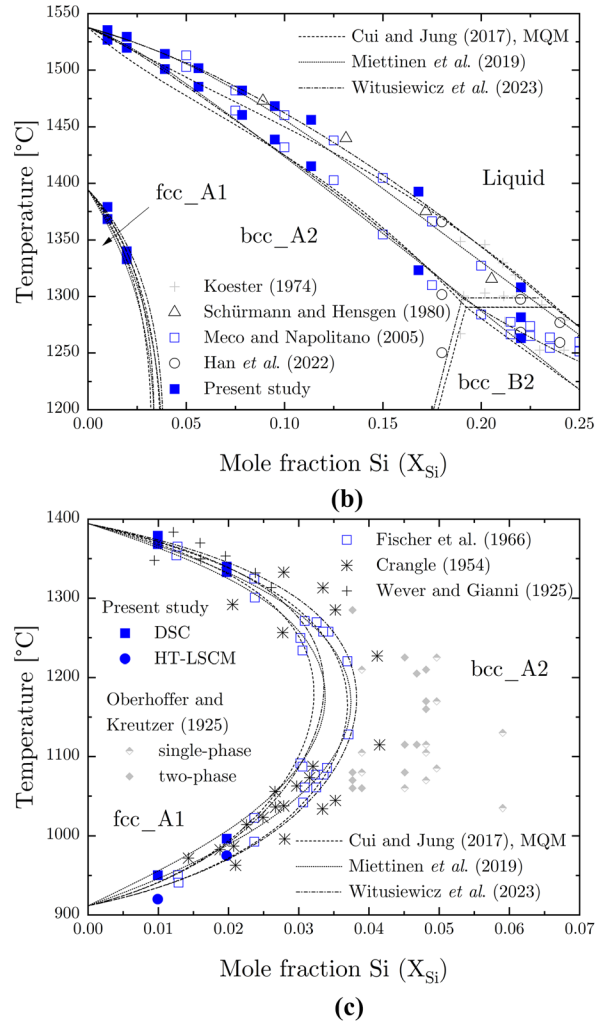
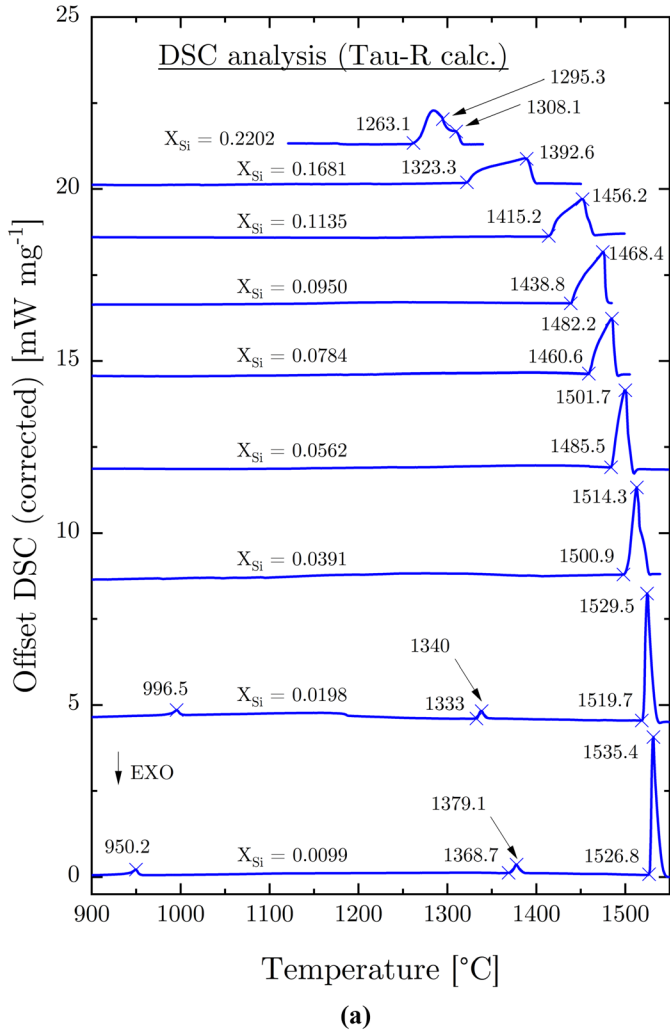


Fig. 4—(a) DSC signals of samples investigated in the present study. Comparison of measured temperatures with literature data^[76,77,79,81,82,108,109] for (b) melting equilibria and (c) the γ -loop along with previous assessments.^[11,12,122] Thermo-Calc 2024 software^[118] was used to represent the phase boundary lines modeled by Witusiewicz *et al.*^[12]

Figure 6 shows the partial excess Gibbs energies of Fe and Si in the melt ($g_i^{\text{ex}} = RT \ln \gamma_i$, $i = \text{Fe or Si}$), where the pure liquids Fe and Si were selected as the reference states, respectively. The calculations were carried out for a temperature of 1600 °C in each case. Similar to the

observations in Figure 5, the partial excess Gibbs energy data also showed significant scatter. Most of the data of Si were measured by EMF,^[31–33,35–37] while Chipman *et al.*^[40] employed Fe/Ag melt equilibration technique and Zaitsev *et al.*^[34] used Knudsen-cell effusion

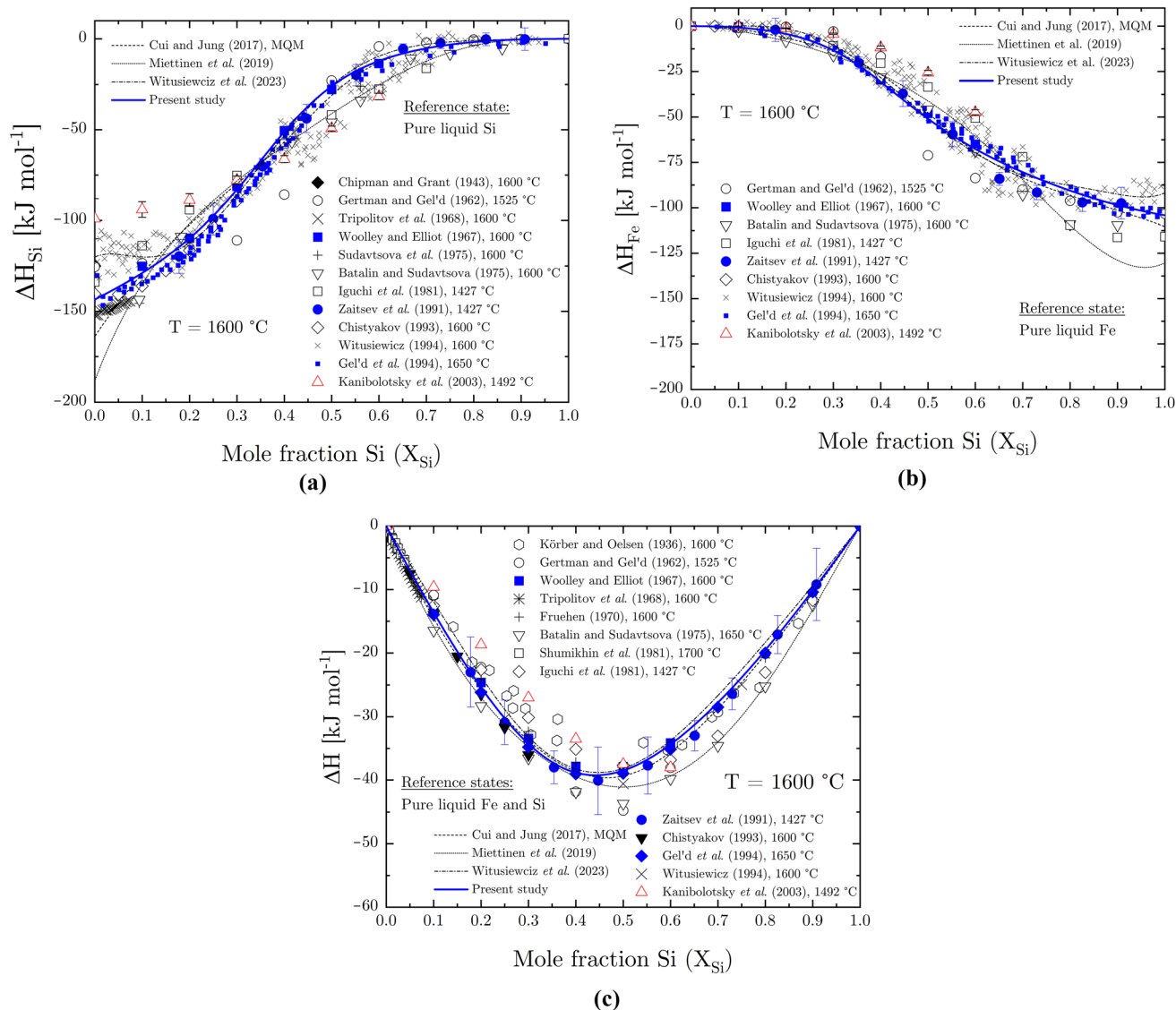


Fig. 5—Enthalpy of the liquid phase. (a) Partial Enthalpy of mixing of Si (ΔH_{Si}), (b) partial Enthalpy of mixing of Fe (ΔH_{Fe}) and (c) integral Enthalpy of mixing of Si (ΔH). The calculations are compared with experimental data from literature and previous thermodynamic assessments.^[11,12,122]

technique. Both non-EMF methods tend to give more negative values than the EMF data. The EMF measurements in Figure 6(a) show a high scatter especially at low Si concentration ($X_{Si} = 0-0.20$), compare for instance the data of Sanbongi and Ohtani^[35] ($g_{Si}^{ex} = -75$ to -60 kJ mol^{-1}) and Sano and Okajima^[36] ($g_{Si}^{ex} = -90$ to -70 kJ mol^{-1}). In Figure 6(b), the original Ag distribution data of Chipman *et al.*^[40] were recalculated using the newly described Ag-Si thermodynamic description of Chevalier.^[163] Within the considerable scatter, it is also an important step to select reliable experimental data for the partial excess Gibbs energy in the present modeling.

Partial excess Gibbs energy and partial enthalpy of mixing are not independent of each other in the MQM, therefore, the selection of two different types of data should have proceeded simultaneously. As the partial excess Gibbs energy eventually determines the Gibbs

energy of the liquid phase, the optimization of the model parameters to calculate the partial excess Gibbs energy in Figure 6 was also carried out by simultaneously calculating liquidus/solidus of Fe-Si binary phase diagram along with the description of the Gibbs energy of bcc_A2 from^[11] (the calculated activities in bcc_A2 with this Gibbs energy resulted in excellent agreement with the activity measurements of Si in bcc_A2 performed by Sakao and Elliott^[43]). The best result was obtained by selecting the measured g_{Si}^{ex} data of Sano and Okajima^[36] out of several other data in Figure 6(a) as well as by considering the data of Chipman *et al.*^[40] and Zaitsev *et al.*^[34] in Figure 6(b): this selection yields the most negative partial excess Gibbs energy of Si (“original model parameters”; blue solid curve in the figures).

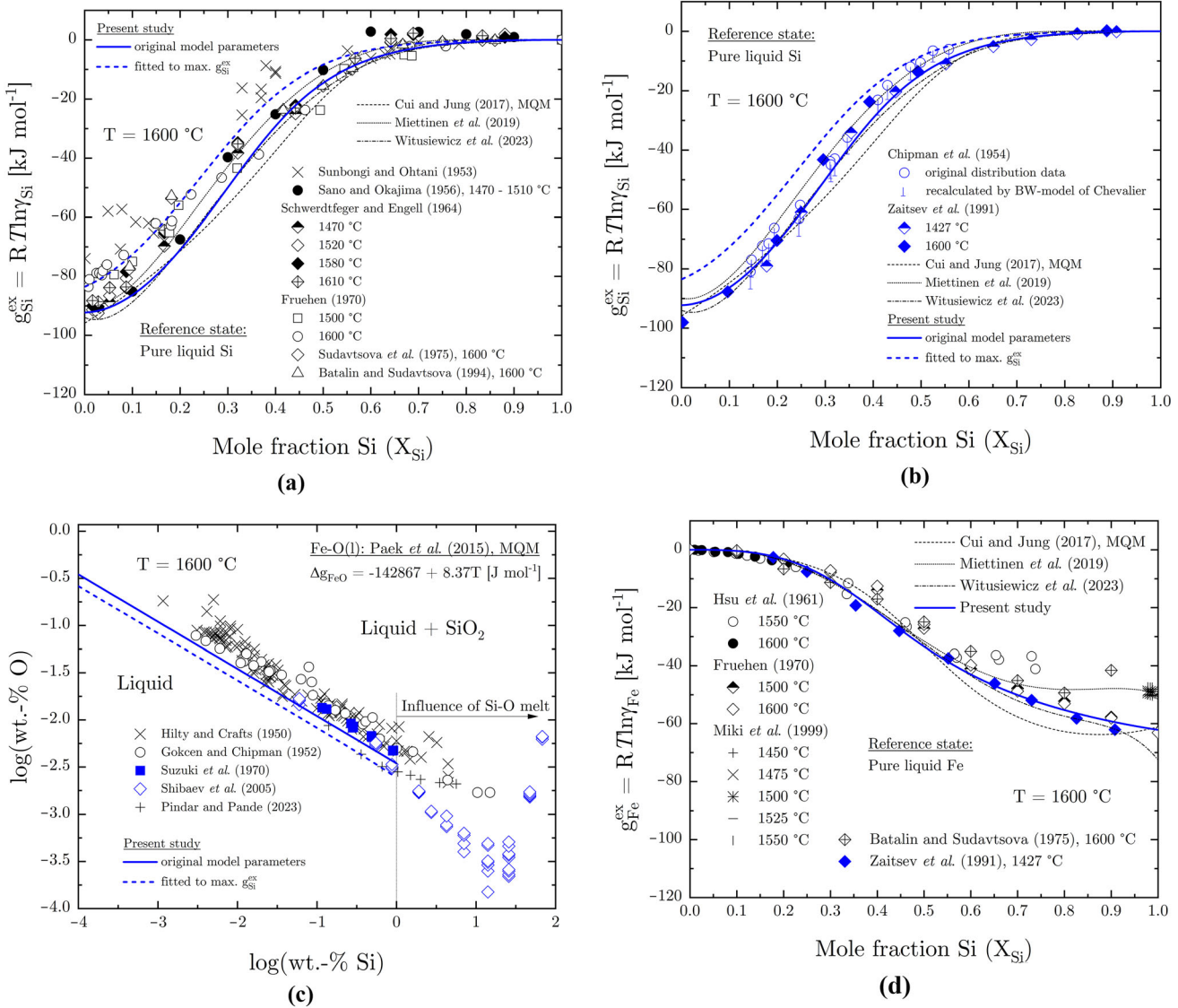


Fig. 6—Calculation of the excess Gibbs energy of the liquid phase. (a) Two optimization strategies using different values published for γ_{Si} (b) comparison with Knudsen-cell effusion measurements^[34] and Fe/Ag equilibration,^[40] (c) evaluation of different calculation strategies based on the well-known Liquid + SiO₂ equilibrium at 1600 °C^[165–169] and (d) results of the optimization with respect to γ_{Fe} along with experimental data.^[31,32,34,39,41] The results are compared with previous assessments.^[11,12,122]

However, it may be also considered that other experimental data, e.g., less negative partial excess Gibbs energy of Si in Figure 6(a), could represent the true partial excess Gibbs energy of Si in the liquid phase. Despite carefully reviewing the available publications, the reason for the discrepancies among the experiments could not be clearly ascertained. In the present study, another attempt was taken to independently justify the selection of $g_{\text{Si}}^{\text{ex}}$ from references.^[34,40] It is the assessment of the Si-O deoxidation equilibria in the Fe-Si-O system, where the activity of Si in the liquid Fe-Si-O is principally determined by the activity of Si in the liquid Fe-Si alloy due to very low O content in the liquid. The Gibbs energy of the ternary liquid composed of Fe-Si-O was formulated by expanding the model equation for the liquid phase described in Sect. “IV–A”. By merging Δg_{FeSi} in the present study, $\Delta g_{\text{FeO}} (= -142867 + 8.37T$

J mol⁻¹) from Paek *et al.*,^[164] and setting Δg_{SiO} null (= 0), the Gibbs energy of ternary liquid composed of Fe-Si-O was estimated. The Gibbs energy of pure SiO₂ (cristobalite) at 1600 °C is well-known ($G_{\text{m}} = -1105.93$ kJ mol⁻¹^[131]). Neglecting the binary Si-O parameter, the liquid/SiO₂ equilibrium can be calculated close to 1 wt pct Si without expecting a too strong influence of the Si-O system.

For validation, a second formulation for Δg_{FeSi} , alongside the original MQM parameters, was developed to represent the maximum values of $g_{\text{Si}}^{\text{ex}}$ [denoted as “max. $g_{\text{Si}}^{\text{ex}}$ ”; shown as the blue dashed line in Figures 6(a) and (b)]. To achieve this, the T -independent parameters in Equation [10] were kept consistent in both MQM formulations, thereby ensuring the same accurate reproduction of ΔH_{Si} , ΔH_{Fe} , and ΔH as shown in Figure 5. The T -dependent terms were then fine-tuned based on

the EMF data from Fruehan,^[30] When comparing now the calculated liquid/SiO₂ equilibrium with experimental data at 1600 °C,^[1165-169] as illustrated in Figure 6(c), it is evident that the liquid phase is less stable relative to SiO₂ than expected. The accuracy of the calculated liquid/SiO₂ was improved when keeping the original MQM parameters (fitted to data reported in references^[34,36,40]). Hence, the original MQM parameters were used in the further optimization procedure. Finally, a distinct improvement for g_{Fe}^{ex} was achieved compared to previous optimizations,^[10-12,122] as demonstrated in Figure 6(d).

Figures 7(a) and (b) show the calculation of the enthalpy of formation (ΔH_f^o) and standard entropy (S_{298}^o) at 25 °C compared to literature data:^[20,42,44-49,52-56] ΔH_f^o and S_{298}^o from Witusiewicz *et al.*^[12] were taken as initial values to fit the phase diagram in the current optimization procedure. Therefore, only minor deviations from this work can be observed. The best agreement was achieved with the results of Acker *et al.*,^[52] though the optimized values are generally within the typical error bars of most calorimetric data given in Figure 7.

Figure 8(a) represents the phase diagram calculated over the whole composition range in comparison with chosen data from the literature^[10,77,82,89-91,95,108,109,112] and the results of the present DSC analysis. The most recent data on non-stoichiometry and phase transition temperatures measured for FeSi and β -FeSi₂^[109] could be excellently reproduced by modifying the CEF parameters as suggested by Witusiewicz *et al.*^[12] The data of Han *et al.*^[109] were not considered in any thermodynamic description yet. The Curie temperature of bcc_A2 follows the measurements of the present study and previous work. A significant improvement of the predicted bcc_A2/liquid phase equilibrium temperatures was achieved by using the MQM, see Figure 8(b). In all cases, the DSC measurements and the reported

data of Mecco and Napolitano^[108] and Han *et al.*^[109] were calculated with high accuracy (± 5 °C). Further, the calculated peritectic transformation (bcc_A2 + liquid \rightarrow bcc_B2) at the highest silicon content (S-IX, $X_{Si} = 0.2202$) only shows a minor deviation of 3 °C. The fcc_A1 parameters of Cui and Jung^[11] were slightly changed to fit the DSC and HT-LSCM data and the experimental results of Fischer *et al.*,^[82] see Figure 8(c). Due to the high-purity samples, the γ -loop equilibrium determined in^[82] was considered as the most reliable already in previous studies.^[79-81] Finally, the solubility of Fe in Si (diamond_A4) was modeled in accordance with the work of Feichtinger^[97] and Wiehl *et al.*^[100] In Figure 8(d), the maximum Fe content is obtained by $X_{Fe} = 2.0 \times 10^{-7}$ at a temperature of 1300 °C.

Table IX compares the calculated invariant temperatures and compositions for each reaction in the entire Fe-Si system with information from the literature presented in Sect. “II”. The data are taken from the comprehensive compilation of Cui and Jung.^[11] The final Fe-Si phase diagram, including the relevant temperatures and marked single-phase regions, is represented in Figure 9.

VI. APPLICATION TO LADLE REFINING OF SI-STEELS

In this section, the new thermodynamic description of the Fe-Si system is used to describe the temperature rise in the ladle during the refining of Si steels in the liquid state. The first part briefly explains the steelmaking process and discusses the available data provided by voestalpine steel division Linz (Austria) as well as their analysis technique. Then stable phases in ferrosilicon

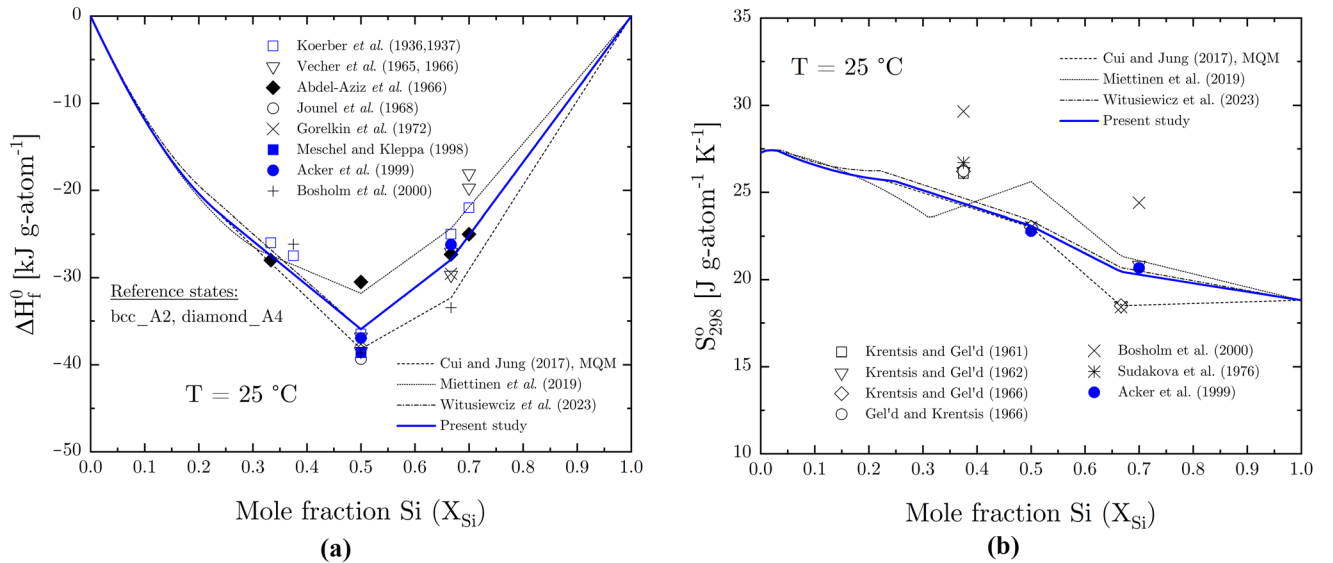


Fig. 7—(a) Calculated enthalpy of formation (ΔH_f^o) and (b) calculated standard entropy (S_{298}^o) along with experimental data:^[20,42,44-49,52-56] from the literature and previous assessments.^[11,12,122] Thermo-Calc 2024 software^[118] was applied for calculations using the assessment by Witusiewicz *et al.*^[12]

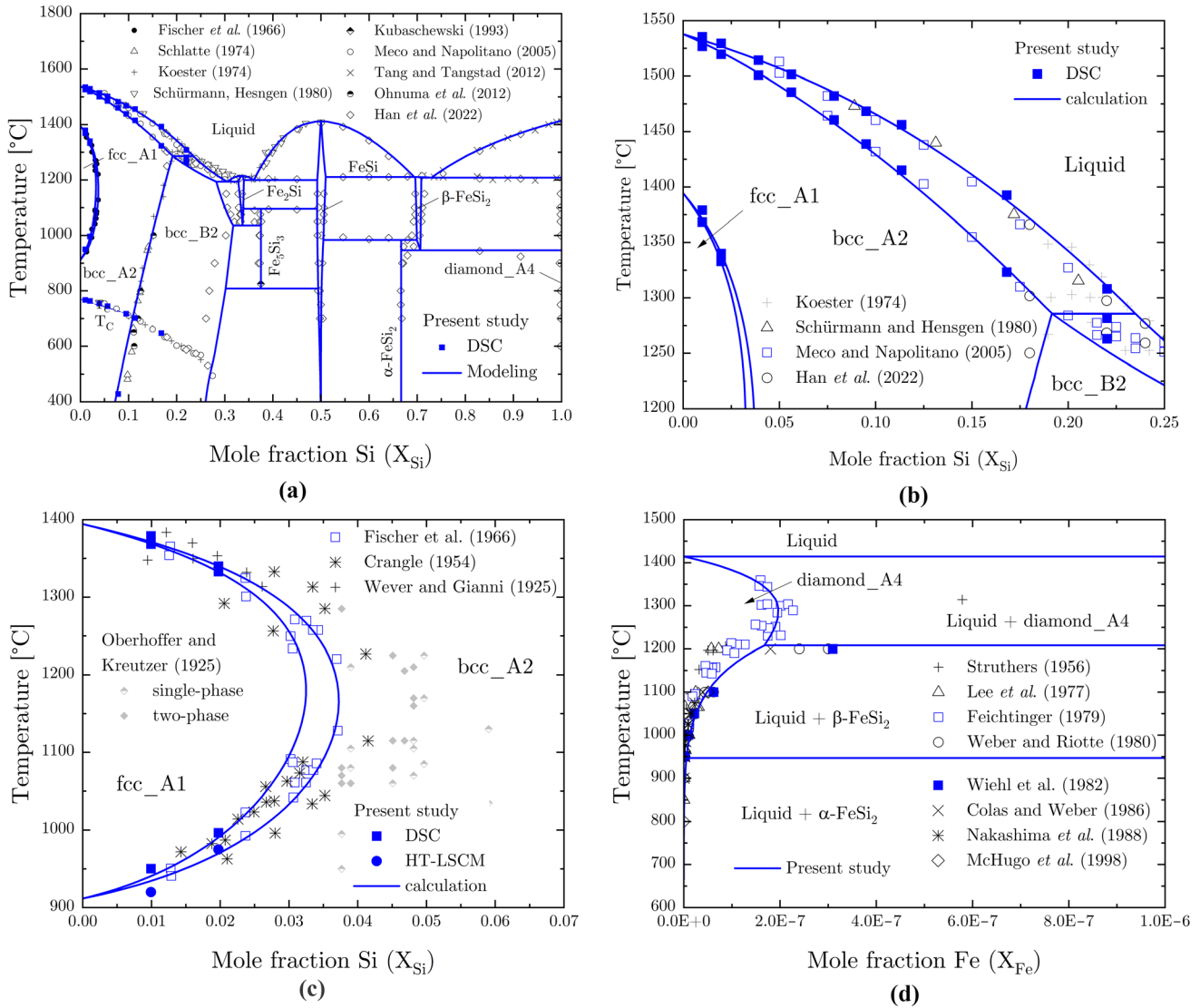


Fig. 8—Phase diagram calculations with the present model parameters. (a) Overall binary Fe-Si system along with data from the literature,^[10,77,82,89–91,95,108,109,112] which were considered in the optimization, and the present DSC analysis, (b) enlarged part of the melting equilibria in the Fe-rich part, (c) detailed representation of the γ -loop and (d) Si-rich part of the phase diagram. Experimental data in (b)–(d) were taken from references 76, 77, 79–82, 96–103, 108, 109.

alloys from the plant are analyzed by XRD to be able to carry out the calculation as practically as possible and the results are compared with the data analysis.

A. Statistical Learning Methods Applied to Steelmaking Process Data

Figure 10 illustrates the secondary refining of silicon steels in the BOF (basic oxygen furnace) - LF (ladle furnace) - RH (Ruhrstahl-Heraeus degasser) steelmaking route, including the steps of sampling, temperature measurements, and alloying conditions. During tapping, only small amounts of pre-deoxidizing agents and slag agents are added to the melt. At this stage, the main objective is to guarantee stable oxygen potential in liquid steel. After sampling and temperature measurement, the ladle is transported to the LF, where purging and heating are performed to homogenize the melt and

to adjust the initial temperature for the vacuum treatment in the RH-degasser. The C content is given by its value at tapping with about 0.03 to 0.04 wt pct. As the oxygen potential is still high, the C content can be reduced to a minimum content (< 30 ppm) via carbon oxidation in the RH-degasser. However, as the thermodynamic equilibrium of the reaction of dissolved C and O to gaseous CO, given by $[C] + [O] = \{CO\}$, is not fully achieved under steelmaking conditions, the O content in the steel remains around 250 to 350 ppm. After first sampling, the melt is therefore fully deoxidized, $2[Al] + 3[O] \rightarrow (Al_2O_3)$ and alloyed with Al up to 0.95 wt pct; the high Al content is also considered beneficial for the magnetic properties of Si sheets.^[170] Finally, the desired Si content (1 to 3 wt pct) is achieved by adding ferrosilicon alloys. Though the steel temperature is dropping during circulation of the melt in the RH treatment, both the deoxidation with Al, and the

Table IX. Summary of Calculated Invariant Temperatures and Compositions Along with Information from Literature^[11]

Type	Reaction	T (°C)	X _{Si} (Phase I) (-)	X _{Si} (Phase II) (-)	X _{Si} (Phase III) (-)	Ref.
Eutectoid	Fe ₅ Si ₃ = bcc_B2 + FeSi	808	0.375	0.302	0.494	PW
		825				66 ^a
		800				70 ^a
		825				68 ^a
		825				112 ^c
		409	0.375	0.2683	0.500	11 ^b
		818	0.375	0.2974	0.500	122 ^b
		825	0.375	0.2949	0.488	12 ^b
Eutectoid	Fe ₂ Si = bcc_B2 + Fe ₅ Si ₃	1036	0.337	0.318	0.375	PW
		1040	0.3329	0.3054		74
		1045	0.3335	0.3120		76
		1044				77
		1045	0.333	0.285	0.375	11 ^b
		1043	0.333	0.292	0.375	122 ^b
		1040	0.339	0.3161	0.375	12 ^b
Peritectoid	Fe ₂ Si + FeSi = Fe ₅ Si ₃	1096	0.339	0.492	0.375	PW
		1020				61
		1045				63
		1030				65
		1030				67
		1030				68
		1046				70
		1046				71
		1090	0.3391			74
		1098	0.3445			76
		1056				77
		1092				109
		1095	0.333	0.50	0.375	11 ^b
		1091	0.333	0.50	0.375	122 ^b
		1080	0.339	0.4903	0.375	12 ^b
		Eutectic	Liquid = bcc_B2 + Fe ₂ Si	1194	0.305	0.282
1190	0.3169			0.299	0.3335	74
1194	0.324			0.304		76
1205	0.3251			0.2981	0.3333	77
1200						112 ^c
1202	0.3049			0.2657	0.333	11 ^b
1197	0.3037			0.2652	0.333	122 ^b
1204	0.3231			0.3064	0.334	12 ^b
Congruent	Liquid = Fe ₂ Si	1215	0.335	0.335		PW
		1251				59
		1215				74
		1215				76
		1210				77
		1212				112 ^c
		1215	0.333	0.333		11 ^b
		1215	0.333	0.333		122 ^b
		1205	0.336	0.336		12 ^b
		Eutectic	Liquid = Fe ₂ Si + FeSi	1199	0.360	0.340
1235						59
1203						61
1239	0.3595					63
1195	0.3320					65
1200						67
1205						71
1202	0.3511			0.3408	0.4939	74
1202	0.346					76
1204	0.3566			0.333		77
1203						112 ^c
1204						109
1202	0.3576			0.333	0.50	11 ^b
1203	0.357			0.333	0.50	122 ^b
1203	0.3386			0.3529	0.4915	12 ^b

Table IX. continued

Type	Reaction	T (°C)	X _{Si} (Phase I) (-)	X _{Si} (Phase II) (-)	X _{Si} (Phase III) (-)	Ref.		
Congruent	Liquid = FeSi	1411	0.50	0.50		PW		
		1443				59		
		1420				61		
		1463				63		
		1410				65		
		1400				67		
		1410				75		
		1410				77		
		1410				112 ^c		
		1404				109		
		1410	0.50	0.50		11 ^b		
		1410	0.50	0.50		122 ^b		
		1411	0.50	0.50		12 ^b		
		Peritectoid	FeSi + β-FeSi ₂ = α-FeSi ₂	983	0.505	0.699	0.667	PW
955				0.6954		104		
998						69		
986				0.6977		73		
982	0.508			0.70		112 ^c		
990						109		
996	0.50			0.699	0.667	11 ^b		
1002	0.50			0.700	0.667	122 ^b		
982	0.506			0.701	0.667	12 ^b		
947	0.707			0.667	~ 1	PW		
Eutectoid	β-FeSi ₂ = α-FeSi ₂ + diamond_A4			960	0.7271			104
		930				69		
		955	0.7061			73		
		940	0.695			75		
		937				95		
		927				112 ^c		
		932				109		
		948	0.699	0.667	~ 1	11 ^b		
		960	0.70	0.667	~ 1	122 ^b		
		937	0.7105	0.667	~ 1	12 ^b		
		Eutectic	Liquid = FeSi + β-FeSi ₂	1210	0.694	0.51	0.696	PW
				1245				59
				1243	0.7078			63
1200	0.6259					64		
1220	0.6193					62		
1213	0.6742					65		
1215						67		
1212						104		
1210	0.6742					69		
1212	0.667					73		
1206	0.67			0.5071	0.692	75		
1212						112 ^c		
1211						109		
1211	0.6674			0.50	0.699	11 ^b		
1204	0.6718	0.50	0.700	122 ^b				
Congruent	Liquid = β-FeSi ₂	1214	0.6897	0.512	0.698	12 ^b		
		1211	0.70	0.70		PW		
		1225	0.6689			62		
		1223	0.7081			65		
		1220				67		
		1216				104		
		1216				69		
		1220	0.705			73		
		1220	0.70			75		
		1220				112 ^c		
		1215	0.70	0.70		11 ^b		
1209	0.70	0.70		122 ^b				
1214.2	0.703	0.703		12 ^b				
Eutectic	Liquid = β-FeSi ₂ + diamond-A4	1208	0.730	0.709	~ 1	PW		

Table IX. continued

Type	Reaction	T (°C)	X_{Si} (Phase I) (-)	X_{Si} (Phase II) (-)	X_{Si} (Phase III) (-)	Ref.
		1245				59
		1245	0.7546			63
		1215	0.7118			64
		1225				62
		1145	0.7410			65
		1145				67
		1207	0.700			104
		1205	0.733			69
		1207	0.7287	0.7247		73
		1202	0.735	0.7142		75
		1207				112 ^c
		1204				109
		1214	0.7186	0.699	~ 1	11 ^b
		1205	0.7259	0.700	~ 1	122 ^b
		1213	0.7321	0.7147	~ 1	12 ^b

PW present work.
^aExperiment, ^bCALPHAD, ^cassessed.

dissolution of Al and Si lead to a significant increase of the ladle temperature, which is confirmed by the last temperature measurement before continuous casting. Here, it must be noted that the major temperature increase results from the melting and dissolution of the ferrosilicon FeSi75 alloy (a mixture of 75 wt pct Si and 25 wt pct Fe), which involves exothermic Si dissolution in liquid Fe (see Figure 5). A possible way to reduce the temperature increase could rely on partial substituting FeSi75 using different alloying materials with a lower Si fraction, e.g., to 65 wt pct (FeSi65). By that, a better heat balance could be achieved before casting, and the process efficiency could be improved.

Comprehensive production data were provided by voestalpine Stahl GmbH in Linz (Austria) to study the influence of Si on the heating effect in the RH plant. By this, the effect of exothermic dissolution of Si in liquid Fe can be quantified under practical operation conditions. Our focus was placed on the data of alloying steps and temperature measurements recorded sequentially during the process. To estimate the drop and/or increase in temperature, the last temperature measurement before decarburization serves as the initial temperature (T_{Start}). Temperatures taken during the RH process ($T_{\text{meas.}}$) are used to assess the heat evolution. The target variable for the statistical evaluation is the difference in temperature between the initial and measured temperatures ($\Delta T = T_{\text{Start}} - T_{\text{meas.}}$).

After data cleansing, a data set with around 3000 observations was obtained, with each observation containing the dependent variable ΔT and various independent variables of process-related influences (such as vacuum treatment time, addition of FeSi75 and/or Al). Multiple Linear Regression (MLR) was used for the statistical analysis:

$$y = \hat{y} + e = \hat{\beta}_1 x_1 + \hat{\beta}_2 x_2 + \hat{s} + \hat{\beta}_n x_n + e \quad [24]$$

where \hat{y} represents the estimated target vector, $\hat{\beta}_n$ is the estimated coefficients of the independent variables, x_n denotes the vector of all values of an independent variable, y is the actual measured values of the target variable, and e is the residual vector. MLR aims to minimize the residual vector by optimally estimating the regression coefficients. The adjusted coefficient of determination R^2_{adjusted} and the forward selection method were used to select the best model regression model. A train-validation-test data split (60–20–20 pct) was conducted to estimate the regression coefficients and evaluate the final model. Additionally, the model training was iterated 100 times, each time with a different seed, resulting in varying splits of observations between the training and validation datasets. This approach enabled the calculation of the standard error of the regression coefficients.

B. Characterization of Ferrosilicon Alloys

Two ferrosilicon alloys (Elkem ASA, Norway) were examined to ensure that the thermodynamic calculations of heat balances in Sect. “VI-C” were as close to real practice as possible. The FeSi75 alloy used as standard at voestalpine Stahl GmbH in Linz and the alternative FeSi65 alloy were characterized both analytically and by X-ray diffraction (XRD). For this purpose, the lumps were milled, and the powder was further examined.

A wet chemical method was applied to determine the concentration of Fe and Si in the ferroalloys. The specimens were dissolved in an HCl and HNO₃ solution. HClO₄ was then added to fully oxidize the Si-bearing substance and confirm its form as SiO₂. The solution was filtered, and the filtrate was used for Fe analysis by ICP-AES. The filter paper with residue was dried, and then flux was added. The mixture was melted in a dry oven at 1000 °C. The ash, contained in a Pt crucible, was weighed. Then, H₂SO₄ and HF were added to volatilize

the SiO₂ fully. The mass change before and after the addition of the H₂SO₄ and HF was taken as the mass of SiO₂, on which the Si content in the alloy was calculated. The results are given by 31.1 wt pct Fe and 68.6 wt pct Si in the FeSi65 alloy and by 23.6 wt pct Fe and 75.3 wt pct Si for FeSi75, respectively. The balances are given for C, P, S, Ti, and Ca. However, in further evaluations, those components will not be considered as the influence on the enthalpy calculations is likely to be negligible.

Additionally, an X-ray Diffraction (XRD) analysis was performed on the two alloys using a Bruker D8-DAVINCI X-ray diffractometer. Cu-K_α radiation with a wavelength of 1.54060 Å was used for the XRD analysis. Figures 11(a) and (b) show the XRD powder analysis of FeSi65 and FeSi75. In both ferroalloys, Si and FeSi₂ are the dominant stable phases, corresponding to the phase diagram plotted in Figure 9. The

diffraction intensity of FeSi₂ decreases with a rising fraction of Si in the alloying material, while Si increases according to the lever rule. It is thus reasonable to include only FeSi₂ and Si in the heat balance calculations for adding ferrosilicon alloys to liquid steel.

C. Quantification of the Temperature Increase During RH Treatment

Figure 12 summarizes the statistical evaluation of the temperature data on the RH plants. The graph shows the temperature difference ($\Delta T = T_{\text{Start}} - T_{\text{meas.}}$) for the duration of the vacuum or the process.

The effect on ladle temperature by adding FeSi75 is shown in Figure 12(a). The amount of ferrosilicon was divided into three groups. Steels with FeSi75 < 500 kg are not specifically alloyed and are degassed in the RH plant only or represent grades, in which deoxidation is carried out after decarburization, e.g. low-carbon (LC) and ultra-low-carbon (ULC) steels. However, the evaluation of the temperature data provides an important parameter, which is the baseline cooling of the steel bath as a function of the process duration. At the beginning of the treatment, the RH snorkels are still somewhat colder, so the steel bath cools down more strongly in the first 30 minutes; the statistical evaluation showed $-1.11 \text{ }^\circ\text{C min}^{-1}$ in “phase I”. The cooling in “phase II” then flattens out due to the reheating of the refractory material; the analysis gives $-0.69 \text{ }^\circ\text{C min}^{-1}$ up to a maximum treatment duration of 75 minutes. The heat of deoxidation and heat of solution by Al, were simply considered in the amount of Al added. If FeSi75 is now alloyed in the RH process, the temperature rises significantly depending on its quantity. By considering the temperature loss of the ladle depending on vacuum treatment time (phase I and phase II) and the temperature increase due to Al addition, the best agreement with the industrial data resulted in a parameter of $(4.73 \pm 0.10) \cdot 10^{-3} \text{ }^\circ\text{C kg}^{-1}_{\text{FeSi}}$. Based on the average

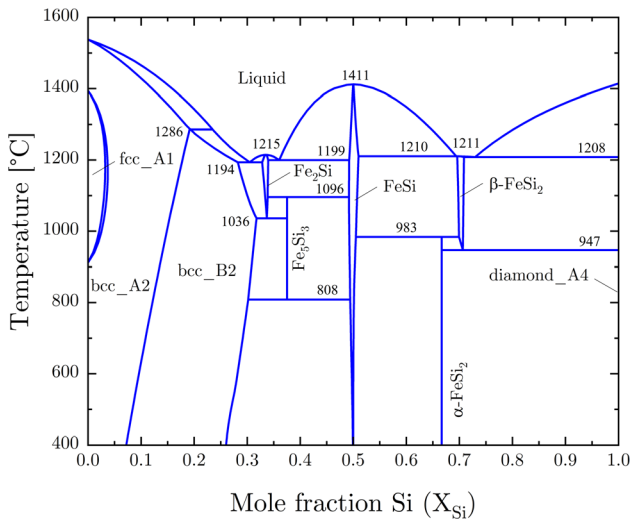


Fig. 9—Complete Fe-Si phase diagram optimized in the present work with calculated invariant temperatures.

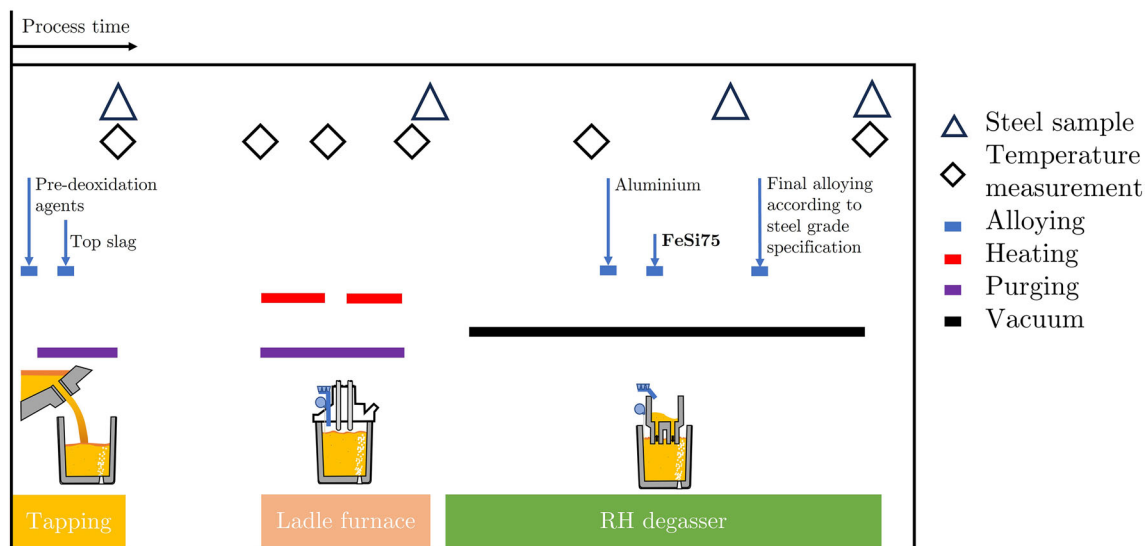


Fig. 10—Schematic representation of secondary steelmaking of electrical steel production in integrated steel mills.

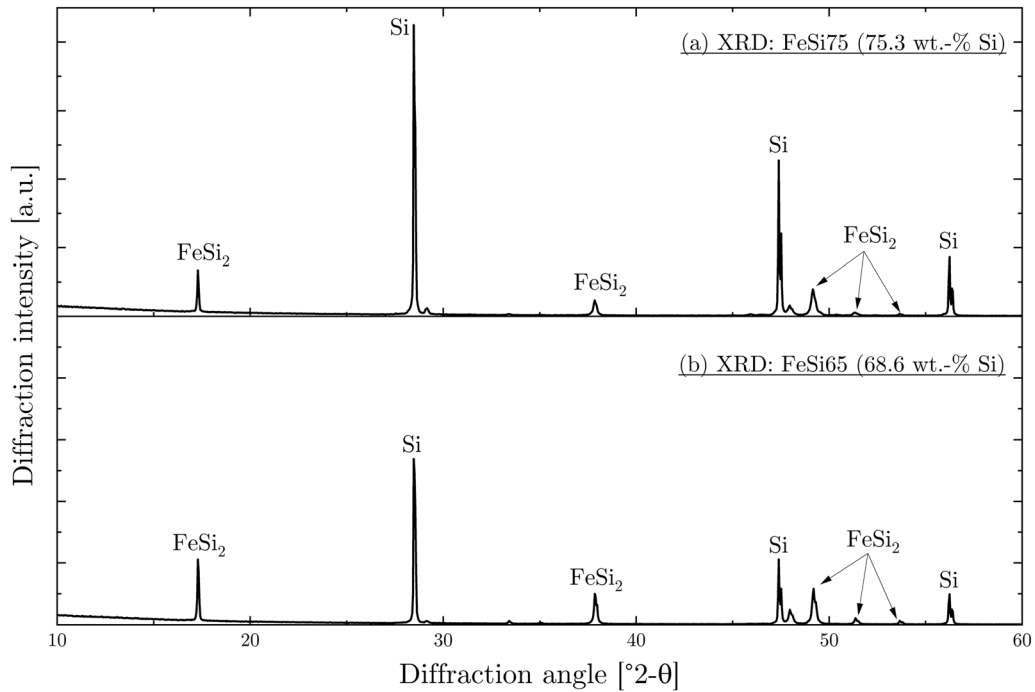


Fig. 11—XRD analysis of phase stabilities of ferrosilicon alloys. (a) FeSi75 containing 75.3 wt pct Si and (b) FeSi65 containing 68.6 wt pct Si.

melt weight of about 172 t, a value of $2.75 \times 10^{-5} \text{ kg}^{-1}_{\text{FeSi}} \text{ t}^{-1}_{\text{steel}}$ is obtained. Compared to the literature values (3×10^{-5} to $7.3 \times 10^{-5} \text{ }^\circ\text{C kg}^{-1}_{\text{FeSi}} \text{ t}^{-1}_{\text{steel}}$), the determined value is rather at the lower limit of the estimated heating effect. If all linear coefficients (ladle cooling, Al and FeSi75 addition) are used for the final temperature calculation, 95 pct of the predictions are within an upper and lower error range of $+12 \text{ }^\circ\text{C}$ and $-13 \text{ }^\circ\text{C}$, see Figure 12(b). A measurement error of $\pm 2 \text{ }^\circ\text{C}$ of the thermocouples used in the steel mill must also be considered. For this large data set, the classic MLR provides excellent correlation with simple statistical analysis of the measurement results, plotted in Figure 12(c).

Thermodynamically, the heating effect of adding FeSi75 to a liquid steel bath was determined using FactSage 8.3,^[131] and the results were critically evaluated against various databases. The calculations were performed under adiabatic conditions ($\Delta H = 0$) considering two different streams. The first stream represents molten steel, assumed to be pure Fe in the liquid reference state at $1550 \text{ }^\circ\text{C}$. The second stream is FeSi75, which, as described in Sect. “VI-B”, consists of the phases Si (diamond_A4) and FeSi2 ($\alpha\text{-FeSi}_2$). According to the lever rule of the phase diagram (Figure 9), the phase weight fractions are $f_{\text{Si}} = f_{\alpha\text{-FeSi}_2} = 0.50$ at 75 wt pct Si in the ferroalloy. Note, that the ladle temperature loss in treatment phase I and phase II as well as the temperature increase by addition of Al were considered in determining the coefficient of FeSi75 alloying in the MLR. By that, it was attempted for the results from statistical learning to be compared with the adiabatic calculations considering only FeSi75 alloying.

The rise in temperature upon adding FeSi75 was determined as a function of the required Si content in the melt. Table X summarizes these calculations for Si contents ranging from 0.50 to 3 wt pct. Using presently optimized model parameters, the thermodynamic calculation shows an almost linear temperature increase of $5 \text{ }^\circ\text{C}$ per ton of FeSi75 added. This increase flattens at higher Si contents. A comparison of the database results with the statistical data analysis shows excellent agreement. However, deviations are observed when compared with literature databases. For instance, the calculation with one database^[122] results in an excessive increase of about $70 \text{ }^\circ\text{C}$ at 3 wt pct Si, which is approximately $40 \text{ }^\circ\text{C}$ higher than industrial data. Conversely, the calculation using the Witusiewicz *et al.*^[12] database shows a negligible increase, with a maximum of $3.4 \text{ }^\circ\text{C}$ at 3 wt pct Si. These discrepancies are attributed to the partial enthalpy of mixing values in the diluted range. The optimization by Cui and Jung^[11] also aligns closely with industrial observations.

The numerical values are shown graphically in Figure 13(a). Additionally, calculations were performed using the current database with the addition of FeSi65 instead of FeSi75. Although the Si content and boundary conditions of the calculations were identical, the lower Si (diamond_A4) fraction in FeSi65 resulted in a lower temperature rise of the steel melt. Thus, a mixture of FeSi75 and FeSi65 appears feasible to precisely control the overheating of the melt to the desired temperature for continuous casting. Figure 13(b) shows a diagram where the temperature increase is plotted against the Si content in the ferroalloy and the desired Si content in the melt. If the Si content in the ferroalloy is low and the Si content in the steel is high, the melt cools

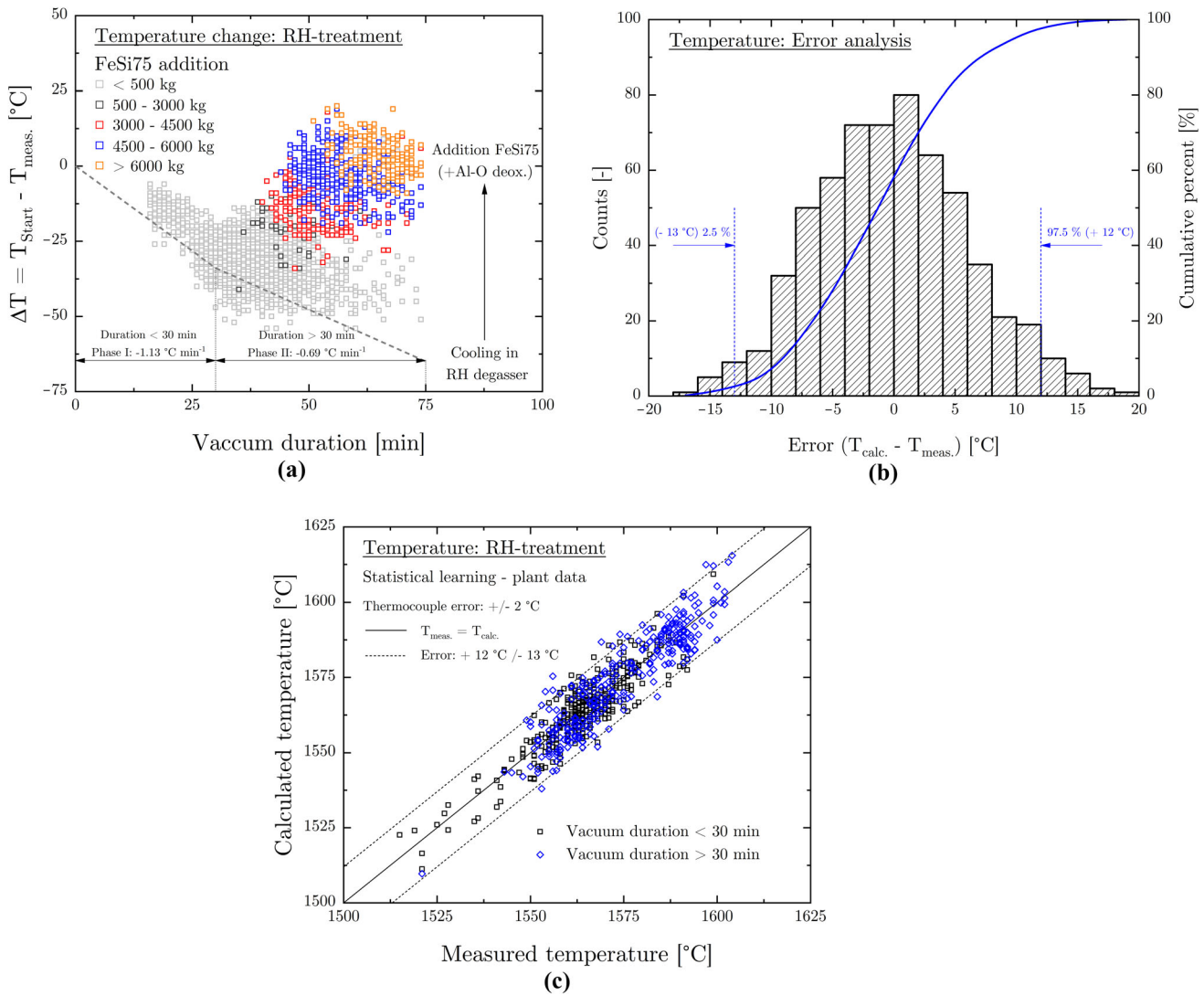


Fig. 12—Statistical data analysis of temperature measured during RH degassing. (a) Temperature drops during vacuum duration when FeSi75 granules are added. (b) Probability density function and cumulative distribution function of error range for temperature prediction. (c) Comparison between measured data and calculated temperatures based on MLR.

Table X. Numerical Values of Adiabatic Calculations to Determine the Reheating Effect of Liquid Fe by Adding FeSi75 to the Bath

Fe (l, 1550 °C) (t)	Si in Liquid Steel (Wt Pct)	FeSi75 (25 °C) (t)	α-FeSi ₂ (s, 25 °C) (t)	Si (s, 25 °C) (t)	ΔT PW ^a (°C)	ΔT PW ^b (°C)	ΔT Ref.[11] (°C)	ΔT Ref.[122] (°C)	ΔT Ref.[12] (°C)
172	0.5	1.2	0.6	0.6	6	5.7	10	16	1
	1	2.4	1.2	1.2	12	11.4	19	30	1.4
	1.5	3.5	1.75	1.75	17	16.6	26	42	2
	2	4.8	2.4	2.4	22	22.7	33	54	2.4
	2.5	5.9	2.95	2.95	26	27.9	39	62	2.8
	3	7.2	3.6	3.6	31	34.1	45	72	3.4

The present work (PW) is compared with results using previous assessments.^[11,12,122]

^aThermodynamic model and ^bdata analysis.

down because the low enthalpy of mixing cannot compensate for the enthalpy required to melt the

ferroalloy. Conversely, this applies to high Si contents in both the steel and the ferroalloy. For better clarity, a dashed line for $\Delta T = 0$ has been added.

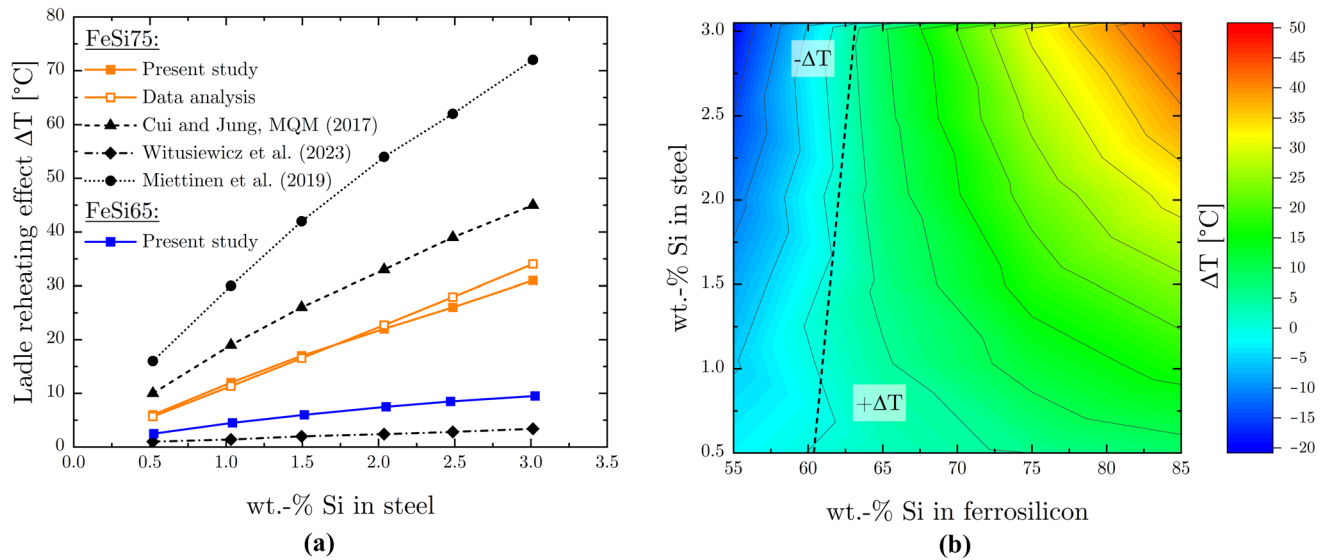


Fig. 13—Results of calculated temperature increase by adding ferrosilicon (25 °C) to liquid steel at 1550 °C under adiabatic conditions. (a) Comparison for FeSi65 and FeSi75 depending on the total Si content in the steel along with MLR observation and with results using other assessments.^[11,12,122] (b) Comprehensive calculations of the temperature increase depending on total Si content in steel and Si content in the ferrosilicon alloy.

VII. CONCLUSION

In the present work, the binary Fe-Si system was reassessed experimentally and by modeling based on the CALPHAD method for application in material design of advanced steel grades and application to processing of silicon steels. The following main improvements were achieved

- The DSC measurements of the melting equilibria in the alloy range of $X_{Si} = 0.01-0.22$ showed a clear deviation from the calculation with existing optimizations. By using the MQM for the liquid phase, an excellent agreement with the measured bcc-A2/liquid phase equilibria could be achieved; the deviation is in the range of ± 5 °C for both the liquidus and the solidus temperature and thus close to the measurement accuracy of the setup used.
- The thermodynamic properties, particularly the S-shaped course of the partial mixture enthalpies (ΔH_{Si} , ΔH_{Fe}), could be better represented using the MQM. The number of model parameters remained identical to the previous work by Cui and Jung.^[11]
- The solubilities of Fe and Si in intermediate silicides could be fitted better to recently published measurement data by Han *et al.*^[109] by modifying already proposed model parameters from the literature.
- An extensive statistical data analysis of temperature measurements during RH treatment of Si steels (172 t ladles) showed that the addition of FeSi75 leads to an increase of 4.73 °C t^{-1} . This value is in excellent agreement with adiabatic calculations using the present optimization (5 °C t^{-1}). The use of other databases from the literature leads to significant differences in the heat balance, which in some cases deviate by more than 40 °C from the industrial measurement data.

The present work is part of the development of a self-consistent thermodynamic database for advanced steels in the multicomponent system Fe-C-Si-Mn-Al.

ACKNOWLEDGMENTS

M.B., P.P. and C.B. gratefully acknowledge the financial support under the scope of the COMET program within the K2 Center “Integrated Computational Material, Process and Product Engineering (IC-MPPE)” (Project No 886385). This program is supported by the Austrian Federal Ministries for Climate Action, Environment, Energy, Mobility, Innovation and Technology (BMK) and for Labour and Economy (BMAW), represented by the Austrian Research Promotion Agency (FFG), and the federal states of Styria, Upper Austria and Tyrol. M.B. and Y.-B.K. acknowledge the financial support of the Brain Pool program funded by the Ministry of Science and ICT through the National Research Foundation of Korea (NRF-2022H1D3A2A01081708). D.K. gratefully acknowledges the funding support of K1-MET GmbH, metallurgical competence center. The research program of the K1-MET competence center is supported by COMET (Competence Center for Excellent Technologies), the Austrian program for competence centers. COMET is funded by the Federal Ministry for Climate Action, Environment, Energy, Mobility, Innovation and Technology, the Federal Ministry for Labour and Economy, the Federal States of Upper Austria, Tyrol and Styria as well as the Styrian Business Promotion Agency (SFG) and the Standortagentur Tyrol. Furthermore, Upper Austrian Research GmbH continuously supports K1-MET. Beside the public funding from COMET, this research project is

partially financed by the Montanuniversitaet Leoben and the industrial partners Primetals Technologies Austria, RHI Magnesita, voestalpine Stahl, and voestalpine Stahl Donawitz.

CONFLICT OF INTEREST

On behalf of the authors, the corresponding author states that there is no conflict of interest.

FUNDING

Open access funding provided by Montanuniversitaet Leoben.

OPEN ACCESS

This article is licensed under a Creative Commons Attribution 4.0 International License, which permits use, sharing, adaptation, distribution and reproduction in any medium or format, as long as you give appropriate credit to the original author(s) and the source, provide a link to the Creative Commons licence, and indicate if changes were made. The images or other third party material in this article are included in the article's Creative Commons licence, unless indicated otherwise in a credit line to the material. If material is not included in the article's Creative Commons licence and your intended use is not permitted by statutory regulation or exceeds the permitted use, you will need to obtain permission directly from the copyright holder. To view a copy of this licence, visit <http://creativecommons.org/licenses/by/4.0/>.

REFERENCES

1. E. Elgamli and F. Anayi: *Appl. Sci.*, 2023, vol. 13, p. 10283.
2. Y. Du, R. O'Malley, and M.F. Buchely: *Appl. Sci.*, 2023, vol. 13, p. 6097.
3. K. Günther, G. Abbruzzese, S. Fortunati, and G. Ligi: *Steel Res. Int.*, 2005, vol. 76, pp. 413–21.
4. H. Tian, Z. Mao, and A. Wang: *J. Iron. Steel Res. Int.*, 2009, vol. 16, pp. 1–6.
5. F. He, A. Xu, H. Wang, D. He, and N. Tian: *Steel Res. Int.*, 2012, vol. 83, pp. 1079–86.
6. Z. Xin, J. Zhang, J. Zheng, Y. Jin, and Q. Liu: *ISIJ Int.*, 2022, vol. 62, pp. 532–41.
7. D. Kavic, M. Bernhard, R. Rössler, and C. Bernhard: in *AISTech—iron and steel technology conference proceedings*, vol. 2024, 2024, pp. 771–84.
8. M. Bernhard, P. Presoly, C. Bernhard, J. Six, and S. Ilie: in *Proceedings 26th International Conference on Metallurgy and Materials*, 2017, pp. 38–44.
9. M. Bernhard, G. Santos, L. Preuler, M. Taferner, G. Wieser, J. Laschinger, S. Ilie, and C. Bernhard: *Steel Res. Int.*, 2022, vol. 93, pp. 2200089.
10. I. Ohnuma, S. Abe, S. Shimenouchi, T. Otori, R. Kainuma, and K. Ishida: *ISIJ Int.*, 2012, vol. 52, pp. 540–48.
11. S. Cui and I.-H. Jung: *Calphad*, 2017, vol. 56, pp. 108–25.
12. V.T. Witusiewicz, O. Stryzhyboroda, S. Vinke, K. Bobzin, and U. Hecht: *J. Alloys Compd.*, 2023, vol. 935, p. 168118.
13. A.D. Pelton, S.A. Degterov, G. Eriksson, C. Robelin, and Y. Dessureault: *Metall. Trans. B*, 2000, vol. 31, pp. 651–59.
14. A.D. Pelton and P. Chartrand: *Metall. Trans. A*, 2001, vol. 32, pp. 1355–60.
15. A.D. Pelton and Y.-B. Kang: *Int. J. Mater. Res.*, 2007, vol. 98, pp. 1–1.
16. Y.-B. Kang and A.D. Pelton: *Calphad*, 2010, vol. 34, pp. 180–88.
17. M. Hillert: *J. Alloys Compd.*, 2001, vol. 320, pp. 161–76.
18. B. Sundman and J. Ågren: *J. Phys. Chem. Solids*, 1981, vol. 42, pp. 297–301.
19. T. Zhou, R. Gani, and K. Sundmacher: *Engineering*, 2021, vol. 7, pp. 1231–38.
20. F. Körber and W. Oelsen: *Mitteilungen aus dem Kaiser-Wilhelm-Institut für Eisenforschung zu Düsseldorf*, 1936, vol. 18, pp. 109–30.
21. J. Chipman and N.J. Grant: *Trans. Am. Soc. Met.*, 1943, vol. 31, pp. 365–79.
22. Y. Gertman and P.V. Gel'd: *Russ. J. Phys. Chem.*, 1962, vol. 36, pp. 788–92.
23. F. Woolley and J.F. Elliott: *Trans. Metall. Soc. AIME*, 1967, vol. 239, pp. 1872–83.
24. A.I. Tripolitov, Y.T. Loginov, A.Y. Stomakhin, and A.F. Filippov: *Izv. Vyssh. Uchebn. Zaved., Chern. Metall.*, 1968, vol. 11, pp. 53–59.
25. V. Shumikhin, A.K. Biletsky, G.I. Batalin, and V.P. Anishin: *Arch. Eisenhuettenwes.*, 1981, vol. 52, pp. 143–46.
26. Y. Iguchi, Y. Tozaki, M. Kakizaki, T. Fuwa, and S. Ban-Ya: *Trans. Iron Steel Inst. Jpn.*, 1982, vol. 68, pp. 633–40.
27. P.V. Gel'd, M.G. Valishev, A.F. Ermakov, and E.D. Pletneva: *Russ. J. Phys. Chem.*, 1994, vol. 68, pp. 1556–58.
28. L.S. Chistyakov, A. Stomakhin, and K.V. Grigorovich: *Metally*, 1993, vol. 4, pp. 27–37.
29. W. T. Witusiewicz: Doctoral Thesis, Kyiv. 1995. p. 254.
30. D.S. Kanibolotsky, O.A. Bieloborodova, N.V. Kotova, and V.V. Lisnyak: *J. Therm. Anal. Calorim.*, 2003, vol. 71, pp. 583–91.
31. R.J. Fruehan: *Metall. Trans.*, 1970, vol. 1, pp. 865–70.
32. G.I. Batalin and V.S. Sudavtsova: *Russ. J. Phys. Chem.*, 1975, vol. 49, pp. 986–88.
33. V.S. Sudavtsova, G.I. Batalin, and V.I. Ul'yanov: *Izv. Akad. Nauk SSSR. Neorg. Mater.*, 1975, vol. 11, pp. 66–71.
34. A.I. Zaitsev, M.A. Zemchenko, and B.M. Mogutnov: *J. Chem. Thermodyn.*, 1991, vol. 23, pp. 831–49.
35. K. Sanbongi and M. Ohtani: *Sci. Rep. Res. Inst., Tohoku Univ.*, 1953, vol. 5, pp. 33–41.
36. K. Sano and K. Okajima: *Mem. Fac. Eng., Nagoya Univ.*, 1956, vol. 8, pp. 254–56.
37. K. Schwerdtfeger and H.-J. Engell: *Arch. Eisenhuettenwes.*, 1964, vol. 35, pp. 533–40.
38. A. Kubo and H. Sakao: *Trans. Iron Steel Inst. Jpn.*, 1968, vol. 54, pp. 314–20.
39. T. Miki, K. Morita, and M. Yamawaki: *J. Mass Spectrom. Soc. Jpn.*, 1999, vol. 47, pp. 72–75.
40. J. Chipman, J.C. Fulton, N. Gokcen, and G.R. Caskey: *Acta Metall.*, 1954, vol. 2, pp. 439–50.
41. C.-C. Hsu, A.Y. Polyakov, and A.M. Samarin: *Izv. Vyssh. Uchebn. Zaved., Chern. Metall.*, 1961, pp. 12–20.
42. R.A. Vecher, Y.I. Gerasimov, and V.A. Geiderikh: *Zh. Fiz. Khim.*, 1965, vol. 39, pp. 1229–32.
43. H. Sakao and J.F. Elliott: *Metall. Trans. A*, 1975, vol. 6, p. 1849.
44. F. Körber, W. Oelsen, and H. Lichtenberg: *Mitt. Kaiser-Wilhelm-Inst. Eisenforsch. Düss.*, 1937, vol. 19, pp. 131–59.
45. A. Abdel-Aziz, A.A. Vertman, and A.M. Samarin: *Izv. Akad. Nauk SSSR. Neorg. Mater.*, 1966, pp. 19–30.
46. B. Journel, J.C. Mathieu, and P. Desre: *C. R. Acad. Sci. Ser. C*, 1968, vol. 266, pp. 773–76.
47. O.S. Gorelkin, A.S. Dubrovin, O.D. Kolesnikova, and N.A. Chirkov: *Zh. Fiz. Khim.*, 1972, vol. 46, pp. 754–55.
48. S. Meschel and O. Kleppa: *J. Alloys Compd.*, 1998, vol. 267, pp. 128–35.
49. O. Bosholm, H. Oppermann, and S. Däbritz: *Z. Naturforsch. B*, 2000, vol. 55, pp. 614–26.
50. P. Schübel: *Z. Anorg. Chem.*, 1914, vol. 87, pp. 81–119.
51. N.N. Serebinnikov, and P.V. Gel'd: *Dokl. Akad. Nauk*, 1954, pp. 695–98.
52. J. Acker, K. Bohmhammel, G. van den Berg, J.C. van Miltenburg, and C. Kloc: *J. Chem. Thermodyn.*, 1999, vol. 31, pp. 1523–36.
53. R.P. Krentsis and P.V. Gel'd: *Fiz. Met. Metalloved.*, 1962, vol. 13, pp. 319–20.

54. R.P. Krentsis, P.V. Gel'd, and G.I. Kalishevich: *Izv. Nats. Akad. Nauk. Resp. Kaz., Ser. Khim.*, 1963, vol. 6, pp. 161–68.
55. R.P. Krentsis, P.V. Gel'd, and G.I. Kalishevich: *Izv. Vyssh. Uchebn. Zaved., Chern. Metall.*, 1963, vol. 6, pp. 146–52.
56. P.V. Gel'd and R.P. Krentsis: *Fiz. Met. Metalloved.*, 1963, vol. 15, pp. 63–71.
57. A. Ferrier and H. Jacobi: *C. R. Acad. Sci. Ser. C*, 1966, vol. 263, pp. 1325–28.
58. M. Ohtani: *Sci. Rep. Res. Inst., Tohoku Univ.*, 1955, vol. 7, pp. 487–501.
59. W. Guertler and G. Tammann: *Z. Anorg. Chem.*, 1905, vol. 47, pp. 163–79.
60. R. Ruer and R. Klesper: *Ferrum*, 1914, vol. 11, pp. 258–61.
61. T. Murakami: *Sci. Rep. Res. Inst., Tohoku Univ.*, 1921, vol. 10, pp. 79–92.
62. T. Murakami: *Sci. Rep. Res. Inst., Tohoku Univ.*, 1927, vol. 1, pp. 475–89.
63. N. Kurnakow and G. Urasov: *Z. Anorg. Allg. Chem.*, 1922, vol. 123, pp. 89–131.
64. M. Bamberger, O. Einerl, and J. Nussbaum: *Stahl Eisen*, 1925, vol. 45, pp. 141–44.
65. J.L. Haughton and M.L. Becker: *J. Iron Steel Inst.*, 1930, vol. 7, pp. 1–8.
66. E.S. Greiner and E.R. Jette: *Trans. Soc. Min. Eng. AIME*, 1937, vol. 125, pp. 473–81.
67. A. Osawa and T. Murata: *J. Jpn. Inst. Met.*, 1940, vol. 4, pp. 228–42.
68. A. Weill: *Rev. Metall.*, 1945, vol. 42, pp. 266–70.
69. K. Wefers: *Metall*, 1963, vol. 17, pp. 446–51.
70. E. Übelacker and P. Lecocq: *C. R. Acad. Sci. Ser. C*, 1966, vol. 262, pp. 793–95.
71. E. Übelacker: *Mem. Etud. Sci. Rev. Metall.*, 1967, vol. 64, pp. 183–90.
72. E. Übelacker: *Colloq. Int. C. N. R. S.*, 1967, vol. 157, pp. 171–73.
73. J.P. Piton and M.F. Fay: *C. R. Acad. Sci. Ser. C*, 1968, vol. 266, pp. 514–16.
74. W. Köster and T. Gödecke: *Z. Metallkd.*, 1968, vol. 59, pp. 602–05.
75. E. Wachtel and T. Mager: *Int. J. Mater. Res.*, 1970, vol. 61, pp. 762–66.
76. W. Köster: *Trans. Iron Steel Inst. Jpn.*, 1974, vol. 14, pp. 387–94.
77. E. Schuermann and U. Hensgen: *Arch. Eisenhuettenwes.*, 1980, vol. 1, pp. 1–4.
78. M. Bernhard, N. Fuchs, P. Presoly, P. Angerer, B. Friessnegger, and C. Bernhard: *Mater. Charact.*, 2021, vol. 174, p. 111030.
79. F. Wever and P. Giani: *Mitt. Kaiser-Wilhelm-Inst. Eisenforsch. Düss.*, 1925, vol. 7, pp. 59–68.
80. P. Oberhoffer and C. Kreutzer: *Arch. Eisenhuettenwes.*, 1929, vol. 2, pp. 449–56.
81. J. Crangle: *Br. J. Appl. Phys.*, 1954, vol. 5, pp. 151–54.
82. W.A. Fischer, K. Lorenz, H. Fabritius, A. Hoffmann, and G. Kalwa: *Arch. Eisenhuettenwes.*, 1966, vol. 37, pp. 79–86.
83. E. Übelacker: *C. R. Acad. Sci. Ser. C*, 1965, vol. 261, pp. 976–79.
84. R.N. Dokken: *Trans. Soc. Min. Eng. AIME*, 1965, vol. 233, pp. 1187–89.
85. D. Meinhardt and O. Krisement: *Arch. Eisenhuettenwes.*, 1965, vol. 36, pp. 293–99.
86. H.H. Ettwig and W. Pepperhoff: *Int. J. Mater. Res.*, 1972, vol. 63, pp. 453–56.
87. G. Inden and W. Pitsch: *Int. J. Mater. Res.*, 1972, vol. 63, pp. 253–58.
88. V.E. Polishchuk and Y.P. Seliskii: *Fiz. Met. Metalloved.*, 1970, vol. 29, pp. 1101–04.
89. G. Schlatter: *Phys. Status Solidi A*, 1974, vol. 23, pp. K91–92.
90. G. Schlatter, G. Inden, and W. Pitsch: *Int. J. Mater. Res.*, 1974, vol. 65, pp. 94–100.
91. G. Schlatter and W. Pitsch: *Int. J. Mater. Res.*, 1975, vol. 66, pp. 660–68.
92. P.R. Swann, L. Grånäs, and B. Lehtinen: *Met. Sci.*, 1975, vol. 9, pp. 90–96.
93. Y. Lecocq and P. Lecocq: *Colloq. Int. C. N. R. S.*, 1967, vol. 157, pp. 165–69.
94. W. Pepperhoff and H.H. Ettwig: *Z. Angew. Phys.*, 1967, vol. 22, pp. 496–99.
95. K. Tang and M. Tangstad: *Acta Metall. Sin.*, 2012, vol. 25, pp. 249–55.
96. J.D. Struthers: *J. Appl. Phys.*, 1956, vol. 27, p. 1560.
97. H. Feichtinger: *Acta Phys. Austriaca*, 1979, vol. 51, pp. 161–84.
98. Y.H. Lee, R.L. Kleinhenz, and J.W. Corbett: *Appl. Phys. Lett.*, 1977, vol. 31, pp. 142–44.
99. E. Weber and H.G. Riette: *J. Appl. Phys.*, 1980, vol. 51, pp. 1484–88.
100. N. Wiehl, U. Herpers, and E. Weber: *J. Radioanal. Chem.*, 1982, vol. 72, pp. 69–78.
101. E.G. Colas and E.R. Weber: *Appl. Phys. Lett.*, 1986, vol. 48, pp. 1371–73.
102. S.A. McHugo, R.J. McDonald, A.R. Smith, D.L. Hurley, and E.R. Weber: *Appl. Phys. Lett.*, 1998, vol. 73, pp. 1424–26.
103. H. Nakashima, T. Isobe, Y. Yamamoto, and K. Hashimoto: *Jpn. J. Appl. Phys.*, 1988, vol. 27, p. 1542.
104. N.K. Abrikosov: *Izv. Sekt. Fiz.-Khim. Anal.*, 1956, vol. 27, pp. 157–63.
105. F.A. Sidorenko, P.V. Gel'd, and P.S. Rempel: *Izv. Vyssh. Uchebn. Zaved., Chern. Metall.*, 1962, vol. 5, pp. 102–08.
106. F.A. Sidorenko and B.S. Rabinovich: *Tr. Ural. Politekh. Inst. im. S. M. Kirova*, 1965, vol. 144, pp. 71–73.
107. E.E. Vainshtein, P.M. Valov, F.A. Sidorenko, and T.S. Shubina: *Fiz. Met. Metalloved.*, 1967, vol. 23, pp. 367–69.
108. H. Meco and R.E. Napolitano: *Ser. Mater.*, 2005, vol. 52, pp. 221–26.
109. K. Han, M. Saito, J. Xia, I. Ohnuma, and R. Kainuma: *J. Alloys Compd.*, 2022, vol. 919, p. 165810.
110. T.G. Chart: *High Temp. High Press.*, 1970, vol. 2, pp. 461–70.
111. T.G. Chart: UK National Physics Laboratory, Teddington, 1982.
112. O. Kubaschewski: *Iron—binary phase diagrams*, Springer, Berlin, 1982.
113. B. Sundman, I. Ohnuma, N. Dupin, U.R. Kattner, and S.G. Fries: *Acta Mater.*, 2009, vol. 57, pp. 2896–908.
114. A.T. Phan, M.-K. Paek, and Y.-B. Kang: *Acta Mater.*, 2014, vol. 79, pp. 1–5.
115. B.-J. Lee, S.K. Lee, and D.N. Lee: *Calphad*, 1987, vol. 11, pp. 253–70.
116. J. Lacaze and B. Sundman: *Metall. Trans. A*, 1991, vol. 22, pp. 2211–23.
117. J. Miettinen: *Calphad*, 1998, vol. 22, pp. 231–56.
118. J.-O. Andersson, T. Helander, L. Höglund, P. Shi, and B. Sundman: *Calphad*, 2002, vol. 26, pp. 273–312.
119. Y. Yuan, F. Pan, D. Li, and A. Watson: *Calphad*, 2014, vol. 44, pp. 54–61.
120. J. Miettinen, S. Louhenkilpi, H. Kytönen, and J. Laine: *Math. Comput. Simul.*, 2010, vol. 80, pp. 1536–50.
121. J. Miettinen, S. Louhenkilpi, V.-V. Visuri, and T. Fabritius: *IOP Conf. Ser.: Mater. Sci. Eng.*, 2019, vol. 529, p. 12063.
122. J. Miettinen, V.-V. Visuri, and T. Fabritius: *Thermodynamic description of the Fe–Al–Mn–Si–C system for modelling solidification of steels*, Acta Universitatis Ouluensis C Technica, University of Oulu, Finland, 2019.
123. K. Shubank and Y.-B. Kang: *Calphad*, 2014, vol. 45, pp. 127–37.
124. P. Gustafson: *Scand. J. Metall.*, 1985, vol. 14, pp. 259–67.
125. M. Bernhard, P. Presoly, N. Fuchs, C. Bernhard, and Y.-B. Kang: *Metall. Trans. A*, 2020, vol. 51, pp. 5351–64.
126. M. Liu, M. Bernhard, M. Kawuloková, J. Walek, M. Kern, S. Zlá, P. Presoly, B. Smetana, M. Tkadlečková, G. Xu, Y.-B. Kang, and C. Bernhard: *J. Mater. Res. Technol.*, 2023, vol. 24, pp. 3534–47.
127. W.J. Boettinger, U.R. Kattner, K.-W. Moon, and J.H. Perepezko: *NIST Recommended Practice Guide*, 2006, Special Publication 960-15.
128. P. Presoly, R. Pierer, and C. Bernhard: *Metall. Trans. A*, 2013, vol. 44, pp. 5377–88.
129. W.-B. Park, M. Bernhard, P. Presoly, and Y.-B. Kang: *J. Mater. Inf.*, 2023, vol. 3, p. 5.
130. M. Bernhard, P. Presoly, C. Bernhard, S. Hahn, and S. Ilie: *Metall. Trans. B*, 2021, vol. 52, pp. 2821–30.
131. C.W. Bale, E. Bélisle, P. Chartrand, S.A. Decterov, G. Eriksson, A.E. Gheribi, K. Hack, I.-H. Jung, Y.-B. Kang, J. Melançon, A.D. Pelton, S. Petersen, C. Robelin, J. Sangster, P. Spencer, and M.-A. van Ende: *Calphad*, 2016, vol. 54, pp. 35–53.

132. E. Moukhina and E. Kaisersberger: *Thermochim. Acta*, 2009, vol. 492, pp. 101–09.
133. H. Yin, H. Shibata, T. Emi, and M. Suzuki: *ISIJ Int.*, 1997, vol. 37, pp. 936–45.
134. H. Yin, H. Shibata, T. Emi, and M. Suzuki: *ISIJ Int.*, 1997, vol. 37, pp. 946–55.
135. H. Shibata, H. Yin, S. Yoshinaga, T. Emi, and M. Suzuki: *ISIJ Int.*, 1998, vol. 38, pp. 149–56.
136. S. Feichtinger, S.K. Michelic, Y.-B. Kang, and C. Bernhard: *J. Am. Ceram. Soc.*, 2014, vol. 97, pp. 316–25.
137. S. Vantilt, B. Coletti, B. Blanpain, J. Fransaer, P. Wollants, and S. Sridhar: *ISIJ Int.*, 2004, vol. 44, pp. 1–10.
138. J. Cejka and S.K. Michelic: *Metals*, 2023, vol. 13, p. 686.
139. C. Liang, G. Song, W. Wang, I.L. Sohn, and J. Zeng: *J. Mater. Res. Technol.*, 2024, vol. 28, pp. 2116–26.
140. H. Yao, Q. Ren, W. Yang, and L. Zhang: *Metall. Trans. B*, 2022, vol. 53, pp. 1827–40.
141. S. Griesser, C. Bernhard, and R. Dippenaar: *Acta Mater.*, 2014, vol. 81, pp. 111–20.
142. S. Griesser, C. Bernhard, and R. Dippenaar: *ISIJ Int.*, 2014, vol. 54, pp. 466–73.
143. I. Sohn and R. Dippenaar: *Metall. Trans. B*, 2016, vol. 47, pp. 2083–94.
144. S.S. Jung and I. Sohn: *Metall. Trans. B*, 2012, vol. 43, pp. 1530–39.
145. G. Kim and I. Sohn: *J. Mater. Res. Technol.*, 2023, vol. 25, pp. 7273–91.
146. N. Fuchs and C. Bernhard: *Mater. Today Commun.*, 2021, vol. 28, p. 102468.
147. M. Kern, M. Bernhard, C. Bernhard, and Y.-B. Kang: *Scr. Mater.*, 2023, vol. 230, p. 115431.
148. C. Bernhard, M. Kern, and M. Bernhard: *Steel Res. Int.*, 2023, vol. 94, p. 2300547.
149. M. Kern, M. Bernhard, Y.-B. Kang, and C. Bernhard: *Acta Mater.*, 2024, vol. 269, p. 119826.
150. Ľ Drozdová, B. Smetana, P. Presoly, V. Novák, M. Machů, M. Bernhard, H. Francová, S. Zlá, L. Řeháčková, and C. Bernhard: *J. Therm. Anal. Calorim.*, 2020, vol. 142, pp. 535–46.
151. M. Kern, M. Bernhard, P. Presoly, D. Brandl, and C. Bernhard: *Berg- Huettenmaenn. Monatsh.*, 2024, vol. 169, pp. 161–66.
152. The GIMP Development Team, 2019., GIMP. <https://www.gimp.org>.
153. A.T. Dinsdale: *Calphad*, 1991, vol. 15, pp. 317–425.
154. M.-S. Kim and Y.-B. Kang: *Calphad*, 2015, vol. 51, pp. 89–103.
155. M.-S. Kim and Y.-B. Kang: *J. Phase Equilib. Diffus.*, 2015, vol. 36, pp. 453–70.
156. M.-A. van Ende and I.-H. Jung: *J. Alloys Compd.*, 2013, vol. 548, pp. 133–54.
157. C. Bernhard, G. Gaiser, M. Bernhard, J. Winkler, M. Kern, P. Presoly, and Y.-B. Kang: *Steel Res. Int.*, 2024, p. 2400494.
158. Y.-B. Kang: *Trans. Iron Steel Inst. Jpn.*, 2020, vol. 60, pp. 2717–30.
159. A.D. Pelton and M. Blander: *Metall. Trans. B*, 1986, vol. 17, pp. 805–15.
160. E.A. Guggenheim: *Proc. R. Soc. Lond. A*, 1935, vol. 148, pp. 304–12.
161. P. Waldner: *J. Phase Equilib. Diffus.*, 2023, vol. 44, pp. 209–19.
162. M. Hillert and M. Jarl: *Calphad*, 1978, vol. 2, pp. 227–38.
163. P.-Y. Chevalier: *Thermochim. Acta*, 1988, vol. 130, pp. 33–41.
164. M.-K. Paek, J.-J. Pak, and Y.-B. Kang: *Metall. Trans. B*, 2015, vol. 46, pp. 2224–33.
165. D.C. Hilty and W. Crafts: *J. Met.*, 1950, vol. 2, pp. 425–36.
166. N.A. Gokcen and J. Chipman: *J. Met.*, 1952, vol. 4, pp. 171–81.
167. K. Suzuki, S. Ban-Ya, and T. Fuwa: *Trans. Iron Steel Inst. Jpn.*, 1970, vol. 56, pp. 20–27.
168. S.S. Shibaev, P.V. Krasovskii, and K.V. Grigorovitch: *ISIJ Int.*, 2005, vol. 45, pp. 1243–47.
169. S. Pindar and M.M. Pande: *Steel Res. Int.*, 2023, vol. 94, p. 2300115.
170. K.M. Marra, L.C. Marra, and V.T.L. Buono: *Mater. Res.*, 2016, vol. 19, pp. 1162–66.

Publisher's Note Springer Nature remains neutral with regard to jurisdictional claims in published maps and institutional affiliations.